



The Extremely Luminous Quasar Survey in the Pan-STARRS 1 Footprint (PS-ELQS)

Jan-Torge Schindler^{1,2}, Xiaohui Fan¹, Yun-Hsin Huang¹, Minghao Yue¹, Jinyi Yang¹, Patrick B. Hall³,
Lukas Wenzl², Allison Hughes¹, Katrina C. Litke¹, and Jon M. Rees⁴

¹Steward Observatory, University of Arizona, 933 North Cherry Avenue, Tucson, AZ 85721, USA

²Max Planck Institute for Astronomy, Königstuhl 17, D-69117 Heidelberg, Germany

³Department of Physics and Astronomy, York University, Toronto, ON M3J 1P3, Canada

⁴Center for Astrophysics and Space Science, University of California San Diego, La Jolla, CA 92093, USA

Received 2019 March 2; revised 2019 April 27; accepted 2019 May 2; published 2019 July 1

Abstract

We present the results of the Extremely Luminous Quasar Survey in the 3π survey of the Panoramic Survey Telescope and Rapid Response System (Pan-STARRS; PS1). This effort applies the successful quasar selection strategy of the Extremely Luminous Survey in the Sloan Digital Sky Survey footprint ($\sim 12,000 \text{ deg}^2$) to a much larger area ($\sim 21,486 \text{ deg}^2$). This spectroscopic survey targets the most luminous quasars ($M_{1450} \leq -26.5$; $m_i \leq 18.5$) at intermediate redshifts ($z \geq 2.8$). Candidates are selected based on a near-infrared *JKW2* color cut using *WISE* AllWISE and 2MASS photometry to mainly reject stellar contaminants. Photometric redshifts (z_{reg}) and star–quasar classifications for each candidate are calculated from near-infrared and optical photometry using the supervised machine learning technique random forests. We select 806 quasar candidates at $z_{\text{reg}} \geq 2.8$ from a parent sample of 74,318 sources. After exclusion of known sources and rejection of candidates with unreliable photometry, we have taken optical identification spectra for 290 of our 334 good PS-ELQS candidates. We report the discovery of 190 new $z \geq 2.8$ quasars and an additional 28 quasars at lower redshifts. A total of 44 good PS-ELQS candidates remain unobserved. Including all known quasars at $z \geq 2.8$, our quasar selection method has a selection efficiency of at least 77%. At lower declinations, $-30 \leq \text{decl.} \leq 0$, we approximately treble the known population of extremely luminous quasars. We provide the PS-ELQS quasar catalog with a total of 592 luminous quasars ($m_i \leq 18.5$, $z \geq 2.8$). This unique sample will not only be able to provide constraints on the volume density and quasar clustering of extremely luminous quasars, but also offers valuable targets for studies of the intergalactic medium.

Key words: galaxies: nuclei – quasars: general

Supporting material: machine-readable tables

1. Introduction

Quasars are excellent tracers of the formation and evolution of highly accreting supermassive black holes (SMBHs) across cosmic time. Their large luminosities not only allow us to detect and study them within the first billion years of the universe (e.g., Fan et al. 2000), but further provide strong background sources with which one can probe the large-scale structure formation of the universe and the nature of the intergalactic medium (IGM) (e.g., Simcoe et al. 2004; Prochaska et al. 2005). The highest-redshift quasars at $z \geq 7$ provide strong constraints on the reionization of the universe (Mortlock et al. 2011; Bañados et al. 2018; Wang et al. 2018b; Matsuoka et al. 2019) and on models of SMBH formation (Volonteri 2012).

Large quasar surveys provide the necessary number statistics to study the evolution of active SMBHs. The Sloan Digital Sky Survey (SDSS; York et al. 2000), the Baryon Oscillation Spectroscopic Survey (BOSS; Eisenstein et al. 2011; Dawson et al. 2013) and the extended BOSS (eBOSS; Dawson et al. 2016) have identified over 500,000 quasars at $z \lesssim 6$ and dozens of quasars at $z > 6$ (Fan et al. 2001, 2003, 2004, 2006; Jiang et al. 2008, 2009, 2016).

Efforts at higher redshifts have also utilized other large surveys like the CFHQS (e.g., Willott et al. 2007, 2010), UKIDSS (e.g., Venemans et al. 2007; Mortlock et al. 2011), VIKING (Venemans et al. 2013), VST-ATLAS (Carnall et al. 2015; Chehade et al. 2018), DES (Reed et al. 2015, 2017, 2019;

Yang et al. 2019a), Pan-STARRS1 (Morganson et al. 2012; Bañados et al. 2014, 2016; Mazzucchelli et al. 2017; Pons et al. 2019) and the DESI Legacy Imaging Surveys (Wang et al. 2018a). The Hyper Suprime-Cam Subaru Strategic program (Aihara et al. 2018) allowed the exploration of the fainter quasar population at intermediate (Akiyama et al. 2018) and high redshifts (Kashikawa et al. 2015; Matsuoka et al. 2016, 2018a, 2018b).

While recent efforts have mainly focused on the high-redshift quasar regime, surveys to identify intermediate-redshift quasars outside the SDSS footprint have been scarce. In particular, the 3π wide area coverage of the Pan-STARRS1 (Panoramic Survey Telescope and Rapid Response System, Kaiser et al. 2002, 2010) survey (PS1; Chambers et al. 2016) provides an excellent opportunity to explore the extremely luminous quasar population ($M_{1450} \lesssim -28$).

While these extremely luminous quasars at intermediate redshift are similarly rare as high-redshift quasars ($10^{-9} \text{ Mpc}^{-3} \text{ mag}^{-1}$; see, e.g., Ross et al. 2013), they are valuable sources to study the He reionization of the universe (Worseck & Prochaska 2011; Worseck et al. 2016), to explore the ionization state of the IGM (Schmidt et al. 2018), to investigate quasar clustering (e.g., Myers et al. 2006), and to constrain the evolution of the bright end of the quasar population (Schindler et al. 2018).

In this work we build on the Extremely Luminous Quasar Survey in the SDSS footprint (ELQS; Schindler et al. 2017, hereafter ELQS1) to discover $z = 2.8\text{--}5$ quasars with $m_i \leq 18.5$ in $\sim 21,486 \text{ deg}^2$ of the PS1 3π footprint.

We first describe the photometry that the quasar selection is based on (Section 2) and give an overview of quasar catalogs in the literature that we use (Section 3). We subsequently present our quasar selection strategy in Section 4 and the construction of the PS-ELQS candidate catalog in Section 5. Section 6 discusses the spectroscopic observations and the data reduction, before we present the PS-ELQS quasar catalog in Section 7. We discuss our results in Section 8 and provide a summary in Section 9. Discovery spectra and tables detailing properties of the newly discovered quasars are available in the Appendices.

We present magnitudes in the AB system (Oke & Gunn 1983), which are corrected for Galactic extinction (Schlegel et al. 1998). All optical passbands refer to PS1, unless otherwise noted. Extinction-corrected magnitudes are denoted by m_x , where x refers to the photometric band, as opposed to extinction-uncorrected magnitudes x . We employ a standard Λ CDM cosmology with $H_0 = 70 \text{ km s}^{-1} \text{ Mpc}^{-1}$, $\Omega_m = 0.3$ and $\Omega_\Lambda = 0.7$, generally consistent with recent measurements (Planck Collaboration et al. 2016).

2. Photometry

2.1. The Wide-field Infrared Survey Explorer

Our quasar selection takes advantage of the *Wide-field Infrared Survey Explorer* (WISE) AllWISE data release, providing infrared photometry over the entire sky at 3.4, 4.6, 12, and 22 μm (W1, W2, W3, W4). AllWISE combines data from the original cryogenic mission and its post-cryogenic extension (Mainzer et al. 2011).⁵ For our selection process we use the W1 (3.4 μm) and W2 (4.6 μm) photometry, for which the AllWISE source catalog achieved 95% photometric completeness for all sources with limiting magnitudes brighter than 19.8, 19.0 (Vega: 17.1, 15.7), respectively. Vega magnitudes were converted to the AB magnitude system using $W1_{\text{AB}} = W1_{\text{Vega}} + 2.699$ and $W2_{\text{AB}} = W2_{\text{Vega}} + 3.339$ and extinction-corrected using $A_{W1}, A_{W2} = 0.189, 0.146$.

2.2. The Two Micron All Sky Survey

We extend the WISE photometry to the near-infrared taking advantage of the Two Micron All Sky Survey (2MASS), which mapped the entire sky in the near-infrared bands J (1.25 μm), H (1.65 μm), and K_s (2.17 μm). The 2MASS point-source catalog (PSC) includes all sources detected with a signal-to-noise ratio $S/N \geq 7$ in one band or $S/N \geq 5$ detections in all three bands. Unfortunately, due to strong confusion of sources closer to the Galactic plane, the photometric sensitivity is a strong function of Galactic latitude. Generally, all sources brighter than 16.7, 16.4, 16.1 (Vega: 15.8, 15.0, 14.3) in the J, H and K_s bands are detected with 10σ photometric sensitivity. However, based on the on-line documentation⁶ we estimate the 10σ limiting magnitudes for higher latitudes to be $J = 17.7, H = 17.5, K_s = 17.1$. Conveniently, the 2MASS PSC has been pre-matched to the WISE AllWISE source catalog. The match corresponds to the closest 2MASS object within a $3''$ radius of the WISE position. All 2MASS Vega magnitudes are converted to the AB system using $J_{\text{AB}} = J_{\text{Vega}} + 0.894, H_{\text{AB}} = H_{\text{Vega}} +$

$1.374, K_{s,\text{AB}} = K_{s,\text{Vega}} + 1.84$ and corrected for Galactic extinction ($A_J, A_H, A_{K_s} = 0.723, 0.460, 0.310$).

2.3. The PS1

We combine the near-infrared/infrared photometry of 2MASS and WISE by DR1 optical photometry from the PS1 3π survey (Chambers et al. 2016). PS1 delivers optical photometry in the $g-, r-, i-, z-,$ and y -bands up to a depth of 23.3, 23.2, 23.1, 22.3, and 21.3 magnitudes ($5\sigma, 3\pi$ stack) over 3π sr of the sky (decl. > -30). Saturation only occurs at magnitudes of $\sim 12-14$, depending on the seeing conditions. The PS1 photometry is nominally on the AB system. All magnitudes are corrected for Galactic extinction ($A_g, A_r, A_i, A_z, A_y = 3.172, 2.271, 1.682, 1.322, 1.087$).

3. Quasar Catalogs in the Literature

To match promising candidates with known quasars from the literature, we make use of the large quasar samples discovered by SDSS I/II (Abazajian et al. 2009), BOSS, and eBOSS published in the SDSS DR7 (DR7Q; Schneider et al. 2010), DR12 (DR12Q; Pâris et al. 2012) and DR14 (DR14Q; Pâris et al. 2018) quasar catalogs.

The quasar selection for the SDSS I/II spectroscopic survey is described in Richards et al. (2002) and selects quasars as outliers of the stellar locus in the $ugri$ and $griz$ color space. Inclusion regions are designed to include quasars in certain redshift ranges which are highly contaminated with stellar sources. The resulting DR7Q includes 100,000 quasars over 9380 deg^2 region of the SDSS DR7 footprint. The BOSS quasar selection (Bovy et al. 2011) was optimized to find quasars in the targeted redshift range of BOSS at $2.2 < z < 3.5$. The newly discovered quasars in BOSS were published in DR12Q. The eBOSS quasar selection (Myers et al. 2015) is based on the XDQSO method (Bovy et al. 2011) and a mid-infrared color cut to provide a uniform quasar sample over 7500 deg^2 with $g_{\text{SDSS}} < 22$ or $r_{\text{SDSS}} < 22$.

The latest version of the SDSS quasar catalog (DR14Q) was then designed to include all quasars observed during any of the stages of the SDSS. Therefore the DR14Q includes nearly all of the DR7Q and DR12Q quasars. All in all, the SDSS discovered more than 500,000 quasars in the northern hemisphere and makes up the majority of the known quasars in the PS1 footprint. We use all three SDSS quasar catalogs mentioned above to match our candidate sample against known sources. Furthermore, the quasar training set for the random forest regression and classification is built from DR7Q and DR12Q quasars.

In addition to the SDSS quasar catalogs we also match our candidates against the Million Quasar Catalog (MQC, version 5.7b; Flesch 2015). The MQC is a compilation of type I and type II active galactic nuclei from all the available literature, including a large fraction of quasar candidates. All quasars from the SDSS quasar catalogs can also be found within the MQC. For the cross-match to our candidate list we exclude all quasar candidates.

J. Yang et al. (2019, in preparation) are also working on a spectroscopic survey of bright quasars at intermediate redshifts similar to PS-ELQS. They are exploring two quasar selections (Wu & Jia 2010; Wu et al. 2012) targeted at $z \approx 2-3$ and at $z \geq 4$ to assess different selection criteria for the upcoming LAMOST quasar survey. The spectroscopic identification

⁵ <http://irsa.ipac.caltech.edu/cgi-bin/Gator/nph-scan?submit=Select&projshort=WISE>

⁶ Figure 7 on https://www.ipac.caltech.edu/2mass/releases/allsky/doc/sec2_2.html.

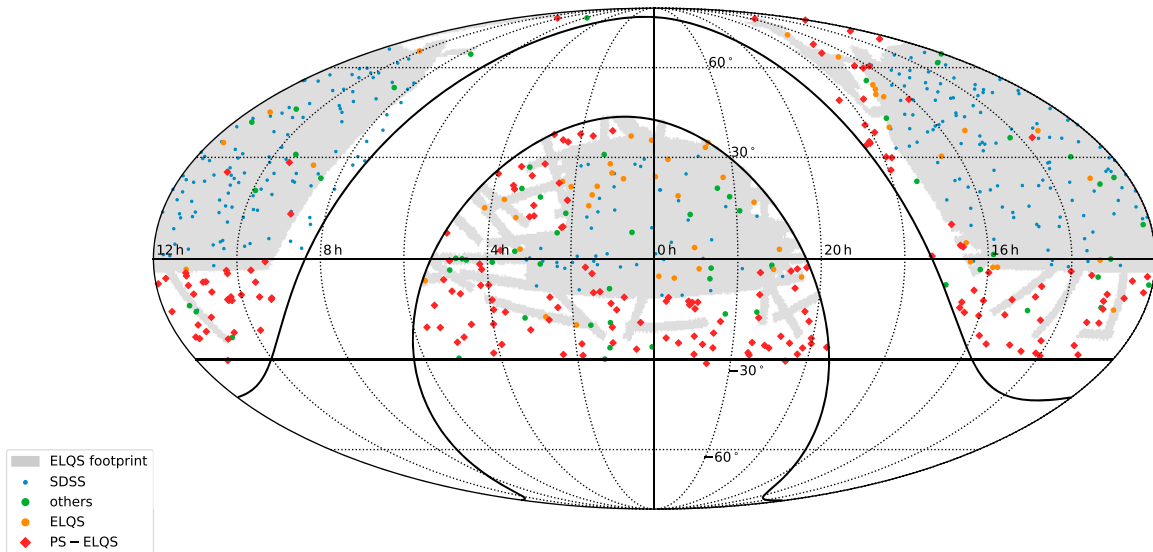


Figure 1. Mollweide projection of the entire sky in equatorial coordinates. The original ELQS footprint is shown in gray. The PS-ELQS footprint covers all area above the thick solid line at decl. = -30 and outside of the two lines outlining the Galactic plane ($|b| \leq 20$). Data points show the position of all 592 quasars in the PS-ELQS quasar catalog (Section 7) colored by their reference.

campaigns were carried out with the Lijiang telescope (2.4 m) and the Xinglong telescope (2.16 m). A number of PS-ELQS candidates were spectroscopically identified by their efforts.

4. The PS-ELQS Quasar Selection

The PS-ELQS quasar selection is in many aspects analogous to the original ELQS quasar selection (see Sections 4–6, ELQS1). However, the optical photometry from PS1 does not provide u -band measurements like the SDSS did. While our initial near-infrared *JKW2* color-cut selection is not affected by this, we lose information on quasars, where the broad emission lines transition from the u -band to the g -band. As a consequence our photometric redshift estimates for quasars at $z \lesssim 3$ might be more unreliable. The additional y -band filter of PS1, which is essential for high-redshift quasar selections, only adds little information for the search of intermediate-redshift quasars.

The following subsections describe the PS-ELQS footprint as well as the individual steps of our quasar selection strategy in detail.

4.1. PS-ELQS Footprint

The ELQS aimed to discover extremely bright, intermediate-redshift quasars, which are very rare. The survey used optical photometry provided by the SDSS over $\sim 12,000 \text{ deg}^2$, excluding the Galactic plane. With the public data release of the PS1 3π survey we can extend our previous efforts to a much larger area and into regions which have not been included in previous quasar surveys. Therefore PS-ELQS is designed to cover the entire PS1 footprint except the Galactic plane ($|b| \leq 20$). Compared to the ELQS footprint we cover an additional $\sim 9600 \text{ deg}^2$, of which the majority ($\sim 5600 \text{ deg}^2$) lies at $-30 \leq \text{decl.} \leq 0$.

Figure 1 shows a Mollweide projection of the entire sky in the equatorial coordinate system. The coverage of the original ELQS is shown in gray. Two thick solid lines map the outline of the Galactic plane ($|b| \leq 20$), which we exclude from our selection. A third solid line at decl. = -30 , shows the southern

border of the PS1 footprint. We effectively select the all the area above decl. = -30 and outside of $|b| \leq 20$ for the PS-ELQS survey. Colored data points show all 592 quasars from the PS-ELQS quasar catalog described in Section 7. The color refers to their source of identification.

We employ the Hierarchical Equal Area isoLatitude Pixelization (HEALPix; Górski et al. 2005) to roughly estimate the area of the PS-ELQS footprint in a similar way to Jiang et al. (2016). HEALPix divides the sky into a grid of curvilinear, equal-sized quadrilaterals. At the lowest resolution the sky is represented by 12 pixels. To create higher-resolution maps each pixel is subdivided into four pixels per resolution level. Therefore the total number of pixels follows $N_{\text{pix}} = 12 \cdot 2^{\text{lvl}}$.

Our coverage estimate is based on 1,918,290 sources selected by our photometric *JKW2* color-cut selection (Section 4.2), which were matched to PS1 according to our quality criteria but without enforcing the extended object rejection. We expect the PS-ELQS footprint to roughly cover $\sim 20,000 \text{ deg}^2$, resulting on average in one source per $\sim 0.01 \text{ deg}^2$. We choose resolutions with $\text{lvl} = 6, 7, 8, 9$ to calculate our coverage maps, resulting in a total number of pixels of 49,152, 196,608, 786,432, and 3,145,728 with $\sim 0.84, 0.02, 0.05,$ and 0.01 deg^2 per pixel. Our coverage estimates for these three resolution levels are 21,697, 21,487, 20,676, and $13,501 \text{ deg}^2$, respectively. There is a large decrease in coverage from $\text{lvl} = 8$ to 9. At the highest resolution the pixel density is approaching the source density and we are effectively oversampling the area.

We adopt a resolution of $\text{lvl} = 7$ with an effective area of $21,486^{+210}_{-833} \text{ deg}^2$ for our final coverage estimate. The uncertainties reflect the differences to the coarser ($\text{lvl} = 6$) and finer ($\text{lvl} = 8$) resolutions.

4.2. Photometric Selection

We begin our photometric selection with the *WISE* AllWISE catalog pre-matched to all sources from the 2MASS PSC. An overview of the selection process is given in Section 5. The source selection is restricted to higher Galactic latitudes

($|b| \geq 20$) to exclude the Galactic plane, where a high source density leads to significant source confusion. The selection further requires $S/N \geq 5$ in the *WISE* W1 and W2 bands and *J*-band detections ($J > 0$) for all objects. At the heart of the near-infrared selection is the *JKW2* color cut (ELQS1),

$$K_{\text{Vega}} - W2_{\text{Vega}} \geq 1.8 - 0.848 \cdot (J_{\text{Vega}} - K_{\text{Vega}}), \quad (1)$$

which allows us to clearly separate quasars at $z < 5$ from the stellar locus in *J–K–W2* color-space.

We obtained 3815,192 sources, which were then further matched to optical photometry from the Pan-STARRS PS1 catalog within a $3''/96$ aperture using the STSCI MAST casjobs interface.⁷ We adopt the flags outlined in Bañados et al. (2014, their Table 6) to ensure the selection of reliable photometry according to the Image Processing Pipeline (Magnier 2006, 2007). The full SQL query to retrieve the PS1 data is provided in Appendix E. We have included a loose criterion to reject extended sources (Section 4.3) in the query to reduce the download size of the data set. The match to the Pan-STARRS PS1 catalog returned a total of 74,318 sources.

The Pan-STARRS PS1 photometry was matched with the AllWISE position. While the AllWISE point-spread function (PSF) is larger than the 2MASS PSF, their average astrometric precision with respect to the U.S. Naval Observatory CCD Astrograph Catalog is similar (2MASS: ~ 80 mas, AllWISE: ~ 87 mas). However, the 2MASS PSC online documentation⁸ notes that stars fainter than $K_{\text{Vega}} \sim 14$ have worse position residuals, which indicates that the extraction uncertainties dominate rather than the uncertainties in the mapping into the IRCS reference frame. As our selection is limited by the depth of the 2MASS survey, and the majority of the pre-matched 3815,192 sources have $K_{\text{Vega}} > 14$, we preferred to use the AllWISE position over the 2MASS position for the cross-match to PanSTARRS PS1.

The optical and near-infrared photometry is extinction-corrected using the python *dustmaps* module (Green et al. 2018) with the values of Schlegel et al. (1998).

4.3. Rejection of Extended Sources

The *JKW2* color cut is highly successful in rejecting stellar contaminants. However, as described in ELQS1, galaxies straddle the color cut and become our main contaminants once the majority of stars are excluded.

We use the absolute value of the magnitude difference (Δm) between the PS1 mean PSF magnitudes (*iMeanPSFMag*) and the PS1 mean aperture magnitudes (*iMeanApMag*) as our main quantity to identify extended sources.

In Figure 2(a) we display two data sets as a function of their magnitude difference, Δm . The first histogram (blue solid line) is calculated from all sources in a region of $b \leq -20$ $120 \leq l \leq 240$ (Galactic coordinates) that passed the *JKW2* color cut and were matched to PS1 photometry according to our criteria above. This corresponds to roughly 2250 deg^2 or $\sim 10\%$ of the total survey area. There are 267,951 sources in this data set, of which 12,579 (15,696) have $\Delta m \leq 0.15$ (0.3). The distribution of the sources as a function of Δm has a minimum around $\Delta m \approx 0.2$, with the majority of sources in the data set exhibiting higher values of Δm . The second data set contains the quasars from the combined SDSS DR7 and

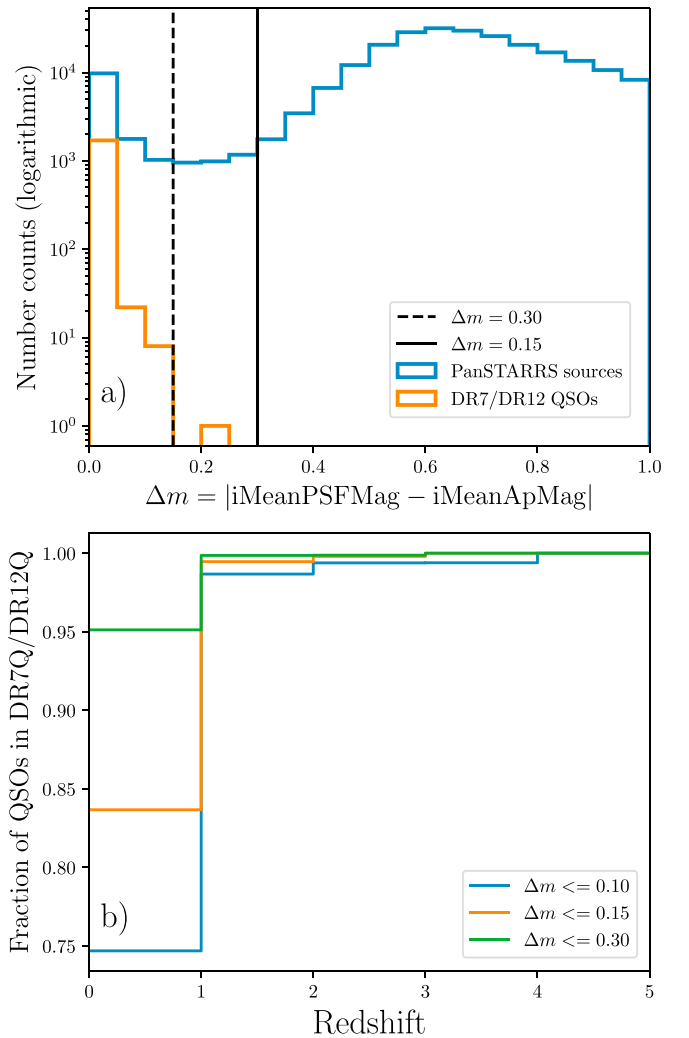


Figure 2. (a) Distribution of PS1 sources (blue) and SDSS DR7Q/DR12Q quasars (orange) as a function of the absolute value of the difference (Δm) between the PS1 mean PSF magnitude and the PS mean aperture magnitude. The PS1 sources are selected by the photometric criteria discussed in Section 4.2 in a region of $b \leq -20$ and $120 \leq l \leq 240$ (Galactic coordinates). The SDSS quasars are restricted to $i \leq 18.5$ and to redshifts $z \geq 2.5$, as targeted in this study. (b) The fraction of bright ($i \leq 18.5$) quasars in the DR7Q/DR12Q included in three different Δm cuts as a function of redshift. At redshifts $z \geq 1.0$ the majority of all quasars are unaffected by the Δm cut.

SDSS DR12 quasar catalogs matched to PS1 photometry. In addition, we only include quasars with $i < 18.5$ and (visually inspected) $z > 2.5$ to restrict the quasar sample to the same magnitude range and redshift range that we target with our selection. All of the remaining 1736 quasars have $\Delta m < 0.3$ and all except one are even included within $\Delta m < 0.15$.

In Figure 2(b) we display the fraction of quasars that are restricted by various cuts on Δm to all SDSS DR7/DR12 quasars with $m_i < 18.5$. It becomes evident that any of the three restrictions on Δm decreases the number of quasars at the lowest redshifts. At redshifts beyond $z \approx 1.0$ the majority of quasars ($> 99\%$) are included even when the stronger restriction of $\Delta m \leq 0.15$ is applied.

For the PS-ELQS quasar selection we thus reject extended sources using $\Delta m < 0.15$ as our main criterion. Based on the SDSS DR7/DR12 quasar samples we estimate that this restriction has a completeness of 99.8% for quasars at

⁷ <http://mastweb.stsci.edu/ps1casjobs/>

⁸ https://old.ipac.caltech.edu/2mass/releases/allsky/doc/sec2_2.html

Table 1

Overview over the Number of Quasars and Stars in the Training Sets

Data Set	DR13 Stars	DR7/DR12 Quasars
Full catalogs	383,966	213,781
Classification		
PS1, $i_{SDSS} < 21.5$	335,591	153,020
PS1+W1W2, $i_{SDSS} < 21.5$	233,137	133,600
PS1+TMASS+W1W2, $i_{SDSS} < 21.5$	169,335	5926
Regression		
PS1+W1W2	...	134,097
PS1+W1W2, $i_{SDSS} < 18.5$...	13,119

$z > 2.5$. After applying the $m_i < 18.5$ magnitude cut and the criterion to reject extended objects to our 74,318 candidates, we retain 43,430 sources.

4.4. Random Forest Redshift Regression and Classification

Random forests (Breiman 2001) are a supervised machine learning technique, that can be efficiently applied to multi-class classification or standard regression problems. The algorithm is non-parametric and avoids the problem of overfitting. In the past random forests have been successfully used on many astronomical data sets (Carliles et al. 2010; Dubath et al. 2011; Richards et al. 2011; Carrasco Kind & Brunner 2013), including quasar classification (Carrasco et al. 2015) and redshift estimation (D’Isanto & Polsterer 2018).

For any supervised machine learning technique, the results of the classifier (or regressor) are highly dependent on the training set. For our purposes we base our training set on quasars from the combined SDSS DR7 and DR12 quasar catalogs as well as on a spectroscopic sample of stars from SDSS DR13. These are essentially the same training sets used in ELQS1, matched to the PS1 source catalog within $3''.96$ to obtain PS1 DR1 photometry. Table 1 provides the total numbers of stars and quasars in the different training sets used below.

After the photometric selection and the extended object rejection our candidate sample is still contaminated by stars and low-redshift ($z < 2.8$) quasars. To enhance our efficiency we use the random forest classifier to reject obvious stellar contaminants and then estimate a photometric redshift with the random forest regressor to select only the $z \geq 2.8$ quasars.

We use the `scikit-learn` (Pedregosa et al. 2011) python implementation of the random forest classifier and regressor with its default parameters unless otherwise noted.

4.4.1. Classification

To further enhance the efficiency of our selection we employ random forest classification. We classify our candidates into four different redshift classes (“vlowz”: $0 < z \leq 1.5$, “lowz”: $1.5 < z \leq 2.2$, “midz”: $2.2 < z \leq 3.5$, “highz”: $3.5 < z$) and five different stellar spectral classes (A, F, G, K, M). The redshift classes are designed to split the quasars at redshifts where emission lines move from one passband into the next redder passband, introducing strong features in the corresponding flux ratios (see also Richards et al. 2015). For evaluation purposes we also summarize all stellar classes

under the “STAR” label and all quasar classes under the “QSO” label, effectively resulting in a binary classification.

We combine the SDSS DR7Q/DR12Q quasars with the SDSS DR13 spectroscopic stars (see ELQS1) matched to PS1 photometry to form the classification training set. Our only requirement is that all objects be brighter than $i_{SDSS} < 21.5$ to exclude very faint objects with substantial photometric uncertainties.

We test the performance of the classification for three subsets of the full training set with different features. The first uses the four adjacent flux ratios (g/r , r/i , i/z , z/y) of the five photometric PS1 bands and the PS1 i -band magnitude as features. For the second and third training set we first include the *WISE* W1 and W2 bands (PS1+W1W2) and for the third we also include all three 2MASS passbands (PS1+TMASS+W1W2). The feature set is expanded accordingly, when we include the *WISE* and 2MASS photometry, by adding the additional flux ratios ($+ [y/W1, W1/W2]$; $+ [y/J, J/H, H/K_s, K_s/W1, W1/W2]$) and the W1 and the J -band magnitude. We require each object in the subsets to have information in all used features (see the constraints in Table 2), resulting in varying number of sources per data set. For each subset we calculate the best combination of hyperparameters for the classifier on a grid of `n_estimators` = [200, 300, 400], `min_samples_split` = [2, 3, 4], and `max_depth` = [15, 20, 25]. As in the case for the photometric redshift regression, we apply five-fold cross-validation on the full training set using 80% of the sources for training and the remaining 20% for validation.

The best hyperparameters are evaluated using the F_1 score (Bishop 2006). The F_1 score, which is also called the traditional F -measure or the balanced F -score, is the harmonic mean of the precision and the recall of the classification:

$$F_1 = 2 \cdot \frac{\text{precision} \cdot \text{recall}}{\text{precision} + \text{recall}}. \quad (2)$$

Here precision (p ; or efficiency) is defined as the ratio of true positives to the sum of true and false positives and the recall (r ; or completeness) is defined as the ratio of true positives to the sum of true positives and false negatives.

Table 2 provides an overview of the best classification results for the three different subsets. The first three columns show the sizes of the training and validation sets for each subset, the constraints on the subset, and the features used. The last three columns provide the precision (p), recall (r) and F_1 measure for the “highz” quasar class as well as the binary classification between quasars (“QSO”) and stars (“STAR”). We would like to stress that only 12 “highz” quasars were included in the PS1+W1W2+TMASS validation set (third row in Table 2) to determine the p , r and F_1 values for the “highz” class, introducing high stochastic uncertainties on those values.

The inclusion of flux ratios beyond the PS1 photometry leads to generally better classification results. On the downside, the sample sizes decrease with the addition of the *WISE* and 2MASS photometry, as we require all objects to have information in all features considered. When the training sets become too small, they will not be able to fully populate the available feature space and thus will lead to worse classifications. Additionally, small validation sets will introduce large errors on the classification metrics. As a result, the recall value and F_1 score of the “highz” class in the PS1+W1W2+TMASS

Table 2
Results of the Random Forest Classification on the Full Empirical Training Set

Training/Validation Size ^a	Constraints	Features ^b	$p/r/F1$ (highz)	$p/r/F1$ (QSO)	$p/r/F1$ (STAR)
390888/97723	PS1 fl.r., $i_{SDSS} < 21.5$	PS1	0.87/0.85/0.86	0.93/0.91/0.92	0.96/0.97/0.97
293389/73348	PS1+W1W2 fl.r., $i_{SDSS} < 21.5$	PS1+W1W2	0.93/0.93/0.93	0.99/1.00/0.99	1.00/0.99/0.99
140208/35053	PS1+TMASS+W1W2 fl.r., $i_{SDSS} < 21.5$	PS1+TMASS+W1W2	1.00/0.67/0.80 (12)	1.00/0.98/0.99	1.00/1.00/1.00

Notes.

^a For the five-fold cross-validation the full data sets are split into a training (80%) and validation (20%) set. We provide the number of objects for each set in this column.

^b We abbreviated flux ratios to “fl.r.” in this column.

9

True label	A	2122 67.50%	953 30.30%	-	-	1	-	2	54	14	
	F	377 1.90%	18371 93.20%	306 1.60%	520 2.60%	4	-	2	106	18	
	G	8 0.20%	3049 82.20%	468 12.60%	144 3.90%	6 0.20%	-	-	32	4	
	K	5 0.10%	843 8.80%	9 0.10%	8464 88.80%	174 1.80%	8 0.10%	-	25	7	
	M	1	12 0.10%	-	153 1.50%	10356 98.30%	1	1	3	5	
	highz	-	1 0.10%	-	4 0.60%	2 0.30%	621 92.80%	3 0.40%	30 4.50%	8 1.20%	
	lowz	-	1	-	-	1	3	4881 74.70%	1155 17.70%	496 7.60%	
	midz	-	18 0.20%	1	5 0.10%	12 0.10%	28 0.30%	675 7.20%	8318 88.90%	301 3.20%	
	vlowz	-	3	-	-	4	9 0.10%	493 4.90%	361 3.60%	9286 91.40%	
			A	F	G	K	M	highz	lowz	midz	vlowz
		Predicted label									

Figure 3. Confusion matrix for the PS1+W1W2 subset (\star in Table 2). The rows show the true labels (classes) of the objects, whereas the columns indicate the predicted labels (classes). Each entry shows the total number of objects of the true row label classified as the predicted column label. The percentages show the fraction of objects in that entry to the total number of objects in the row. The entries are color coded to highlight the entries with the majority of objects in each row.

set is worse than in the other two subsets, although more features are included.

Hence, we adopt the PS1+W1W2 subset as the best training and feature set for our classification problem (marked with \star in Table 2). It achieves the best classification results of all three subsets. The best hyperparameters for this set were evaluated to be $n_{\text{estimators}} = 400$, $\text{min_samples_split} = 4$, and $\text{max_depth} = 25$.

A helpful visualization to understand the classification result is the confusion matrix. Each row of the matrix marks the true class of the objects within it, which are predicted to belong to different classes according to the columns of the matrix. The diagonal entries show the number of correctly classified objects, while all off-diagonal entries show the numbers of incorrectly classified objects. It provides a good overview of which classes are commonly confused and which can be separated easily with the features supplied to the classifier.

We display the entire confusion matrix for the PS1+W1W2 subset (\star) in Figure 3. The individual entries show the number of objects belonging to the row class (true label) and classified as the column class (predicted label). The percentages below each entry are with respect to the total number of objects in the true class (full row). Therefore the percentages of the diagonal entries show the completeness with respect to its row/column label.

The quasar and star classes are well separated. The largest number of stellar contaminants enter in the “midz” quasar class ($2.2 \leq z \leq 3.5$). This is one redshift range, where the quasar distribution overlaps strongly with the stellar locus in optical color space. Indeed, the majority of quasars misclassified as stars also stem from this redshift class. Within the quasar classes “midz” and “lowz” quasars show the highest level of confusion with each other.

4.4.2. Photometric Redshift Regression

Our selection process rejects stars with the *JKW2* color cut and galaxies due to their large difference in mean PSF and aperture magnitudes. Therefore, quasars at $z < 2.8$ become the dominant contaminants. We use random forest regression to calculate photometric redshifts, z_{reg} , and then select quasar candidates with $z_{\text{reg}} \geq 2.8$.

The training set includes all SDSS DR7/DR12 quasars with full PS1 and *WISE* W1 and W2 photometry. We also build a smaller subset, limiting the full quasar training set to $i < 18.5$.

The features used for the random forest regression are the six adjacent flux ratios (g/r , r/i , i/z , z/y , $y/W1$, $W1/W2$) from the five photometric bands of PS1 in addition to W1 and W2. We further add the PS1 *i*-band magnitude and the W1 magnitude to the feature set. As discussed in ELQS1, including 2MASS photometry dramatically reduces the number of training objects and therefore does not allow for sufficient training in the large feature space.

We perform grid searches on the full training set and the magnitude-limited subsample to determine the hyperparameters of the best regression model. The grid of hyperparameters includes the number of binary trees ($n_{\text{estimators}} = [200, 300, 500]$), the minimum number of samples to be split ($\text{min_samples_split} = [2, 3, 4]$), and the maximum depth of the tree ($\text{max_depth} = [15, 20, 25]$). To test the hyperparameters we use five-fold cross-validation on the full training set using each time 80% of the sources for training and the remaining 20% for validation.

The best hyperparameters are evaluated using the standard R^2 regression score,

$$R^2 = 1 - \frac{\sum_i (z_{\text{spec},i} - z_{\text{reg},i})^2}{\sum_i (z_{\text{spec},i} - \bar{z})^2}, \quad (3)$$

where $z_{\text{spec},i}$ are the true redshifts, \bar{z} is the mean of all $z_{\text{spec},i}$, and the predicted redshift values are denoted by $z_{\text{reg},i}$. The other common metric in the literature assesses the goodness of the redshift estimation with redshift-normalized residuals ($\delta z = |z_{\text{reg}} - z_{\text{spec}}| / (1 + z_{\text{spec}})$). Most studies report the fraction of quasars in the validation set with residuals smaller than a given threshold e :

$$\delta_e = \frac{N(|z_{\text{reg},i} - z_{\text{spec},i}| < e \cdot (1 + z_{\text{spec},i}))}{N_{\text{tot}}}, \quad (4)$$

where N_{tot} denotes the total number of quasars in the validation set. Residual thresholds of $e = 0.1, 0.2$, and 0.3 are typically chosen in this context.

We show the best results of the regression grid search for the full quasar training set and the magnitude-limited subsample in Table 3. While the magnitude-limited subset (second row) achieves slightly better results, the training set is reduced to 10% of its full size. In addition, it will be additionally biased against higher-redshift quasars, because they are generally fainter. Therefore we adopted the full quasar training set (marked with \star in Table 3). The best hyperparameters for this case are $\text{min_samples_split} = 2$, $n_{\text{estimators}} = 500$, and $\text{max_depth} = 25$. The resulting distribution of spectroscopic redshifts to random forest regression redshifts in the validation set are shown in Figure 4. While the results at $z \gtrsim 3$ are mostly within the region of $\Delta z = |z_{\text{spec}} - z_{\text{reg}}| \leq 0.3$, a larger distribution of outliers persists at lower redshifts.

Table 3
Results of the Photometric Redshift Estimation Methods

Data Set	Training/Validation Size ^a	Constraints	Features	$\delta_{0.3}$	$\delta_{0.2}$	$\delta_{0.1}$	σ^b	R^2	
DR7DR12Q	107277/26820	PS1+W1W2 fl.r.	PS1+W1W2	0.95	0.91	0.79	0.352	0.817	*
DR7DR12Q	10495/2624	PS1+W1W2 fl.r., $i < 18.5$	PS1+W1W2	0.98	0.95	0.88	0.265	0.883	

Notes.

^a For the five-fold cross-validation the full data sets are split into a training (80%) and validation (20%) set. We provide the number of objects for each set in this column.

^b Standard deviation of the residual of the photometric redshift estimate (regression redshift) and the measured spectroscopic redshift.

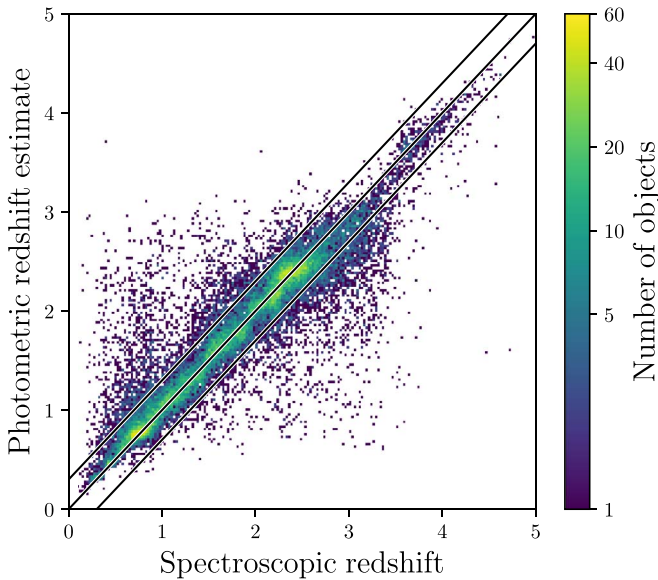


Figure 4. Distribution of quasars in the validation set (* in Table 3) as a function of photometric redshift estimate (regression redshift) and measured spectroscopic redshift, color coded by the number of objects per bin. The three solid black lines illustrate the $\Delta z = |z_{\text{spec}} - z_{\text{reg}}| = 0$ diagonal and the $\Delta z \leq 0.3$ region.

5. Construction of the PS-ELQS Quasar Candidate Catalog

We provide an overview of the candidate selection process in Figure 5 and Table 4. The selection process begins with the parent sample of 2MASS and WISE AllWISE sources, which pass the JKW2 color cut and have reliable photometry ($S/N(W1) \geq 5$, $S/N(W2) \geq 5$, $J > 0$). We then match these sources to the PS1 photometry within a $3''.96$ aperture, requiring the objects to be brighter than $i = 19.0$ and fulfil $\Delta m \leq 0.3$. Furthermore all objects have to satisfy a range of quality flags. The full SQL query is shown in Appendix E. After we retrieved the PS1 photometry for all remaining sources (74,318), we apply the more stringent rejection of extended sources ($\Delta m \leq 0.15$) and restrict the sample to all sources with $i \leq 18.5$.

At this point we run the random forest regression and classification. The regression provides us with a regression redshift z_{reg} , our photometric redshift estimate. The classification determines the most likely class of the object (`rf_mult_class_pred`) and the summed probability of the object belonging to any of the quasar classes (`rf_qso_prob`). All objects that are generally classified as quasars (“QSO”), according to the binary classification, and have regression redshifts of $z_{\text{reg}} \geq 2.8$, form the PS-ELQS candidate sample.

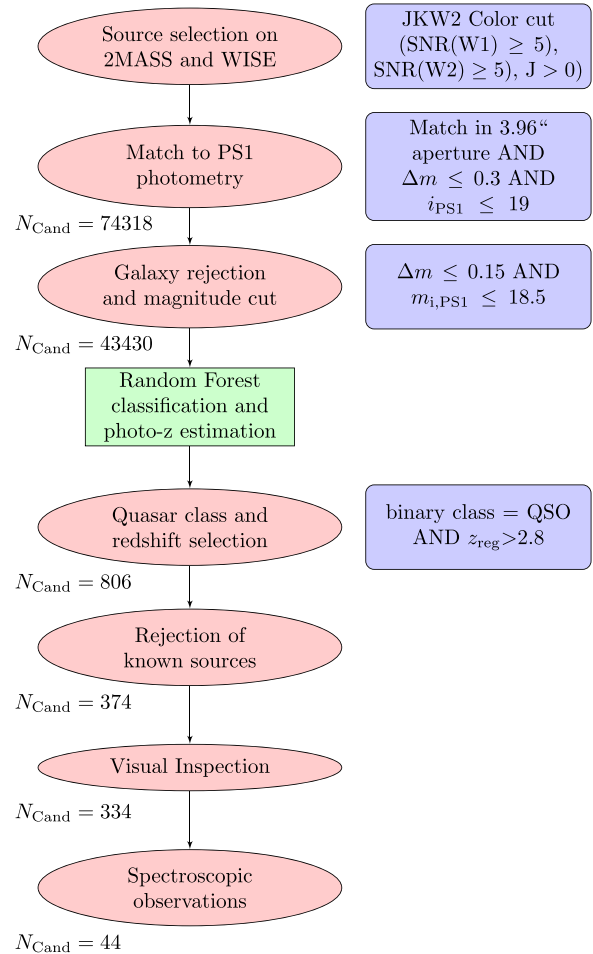


Figure 5. Flowchart of the PS-ELQS quasar candidate selection.

The PS-ELQS candidate sample selects a total of 432 known quasars from the literature, including 70 sources observed as part of the ELQS, which are then excluded from the candidate sample along with all other known sources. We visually inspect all unknown candidates for unreliable photometry. We reject all candidates whose PSF is blended with nearby sources, where image artifacts are evident or the source seems to be extended. After the exclusion of known quasars and the rejection of 40 candidates with unreliable photometry, the “good” PS-ELQS candidate sample has a total of 334 objects. These candidates are then prioritized according to the criteria described in Table 5.

Table 4
PS-ELQS Candidate Selection

<i>WISE</i> +2MASS+PS1 parent sample (<i>JKW2</i> color cut, $i < 19.0$, $ \Delta m < 0.3$)	74318
Photometric sample ($i < 18.5$, $ \Delta m < 0.15$)	43430
PS-ELQS candidate sample ($z_{\text{reg}} \geq 2.8$ and class = “QSO”)	806
Known QSOs in the literature in the candidate sample	432
Known $z \geq 2.8$ QSOs in the literature in the candidate sample	402
Observed ELQS sources in the candidate sample	70
Known $z \geq 2.8$ ELQS QSOs in the candidate sample	54
Good PS-ELQS candidates (excluding bad photometry and known sources)	334
Good PS-ELQS candidates observed	290
Remaining good PS-ELQS candidates	44
New PS-ELQS quasars	218
New PS-ELQS quasars at $z \geq 2.8$	190

Table 5
PS-ELQS Quasar Candidates and Their Selection Priorities

Priority	Criteria	Good PS-ELQS Candidates (44 remaining)
1	$3.5 \leq z_{\text{reg}}$ and $m_i \leq 18.0$	53 (3)
2	$3.0 \leq z_{\text{reg}} \leq 3.5$ and $m_i \leq 18.0$	49 (5)
3	$(2.5 \leq z_{\text{reg}} \leq 3.0$ and $m_i \leq 18.0)$ OR $(3.5 \leq z_{\text{reg}}$ and $18.0 < m_i \leq 18.5)$	122 (12)
4	$3.0 \leq z_{\text{reg}} \leq 3.5$ and $18.0 < m_i \leq 18.5$	59 (8)
5	$2.5 \leq z_{\text{reg}} \leq 3.0$ and $18.0 < m_i \leq 18.5$	46 (16)
10	all the remaining candidates	5

Spectroscopic observations could successfully identify 290 good PS-ELQS candidates, of which 190 are quasars at $z \geq 2.8$. A total of 44 good PS-ELQS candidates have not yet been observed, but are targeted in future observing campaigns. A list of the remaining PS-ELQS candidates is given in Table 10 in Appendix D.

6. Spectroscopic Follow-up Observations and Data Reduction

Dedicated observational campaigns for the PS-ELQS began in fall 2017 after the candidate selection was frozen in. Observations were completed in 2018 June. In this section we will describe the observational setups and the data reduction procedure.

6.1. SOAR

The focus of this quasar survey was the mostly unexplored area of the PS1 3π survey between Galactic latitudes of $-30 < b < 0$. Therefore the majority of our observations were carried out with the Goodman High Throughput Spectrograph (Goodman HTS; Clemens et al. 2004) on the Southern Astrophysical Research (SOAR) Telescope (4.1 m). Spectra were taken in 2017 October 6–10, 2018 January 22–24, 2018 April 4–6, and 2018 June 2–4. We used the 400 g mm^{-1} grating with central wavelengths of 6000 and 7300 Å. The first setup utilized the GG-385 blocking

filter, whereas we used the GG-495 blocking filter for the second setup. The spectra have a wavelength coverage of $\sim 4000\text{--}8000$ and $\sim 5300\text{--}9300$ Å for the two different central wavelengths. We chose slit widths of $1''.0$ or $1''.2$ dependent on the weather conditions, resulting in spectral resolutions of $R \approx 830$ and $R \approx 690$, respectively. Exposure times varied between 3 and 15 minutes depending on the target magnitude and the atmospheric transparency.

6.2. VATT Observations

Identification spectroscopy in the northern hemisphere was carried out with the VATTSpec spectrograph on the Vatican Advanced Technology Telescope (VATT). Using the 300 g mm^{-1} grating blazed at 5000 Å in first order, we achieved a resolution of $R \sim 1000$ ($1''.5$ slit) and a coverage of ~ 4000 Å around our chosen central wavelength of ~ 5850 Å. Targeted PS-ELQS observations were conducted in 2017 November 7–12, 2018 March 19–21, and 2018 May 17–18. Depending on the source and the conditions the exposure times varied between 15 and 30 minutes.

6.3. MMT Observations

We followed up our newly discovered quasars with the Red Channel Spectrograph on the MMT. We used the 300 g mm^{-1} grating blazed at 1st/4800 Å with central wavelengths of 5655, 5570, and 5900 Å. The grating has an approximate coverage of 3310 Å and achieves a resolution of $R \approx 400$ to 300 for the $1''.25$ and the $1''.5$ slits. Depending on the source and the weather conditions we chose exposure times of $\sim 3\text{--}15$ minutes per spectrum. Observations were taken in 2017 October 20–21, 2017 November 16, and 2018 May 14.

6.4. Data Reduction

We reduced the spectra with the long-slit reduction methods within the IRAF software package (Tody 1986, 1993). Standard bias subtraction, flat-field correction, and sky subtraction were applied. Sky subtraction and spectral extraction were done using the `apall` routine with optimal extraction (weights = variance) and cosmic ray reduction. The resulting low- to medium-S/N spectra allowed quasars to be easily identified by their broad emission lines. The wavelength calibration was based on internal lamps, and spectral fluxes were initially calibrated using at least one spectrophotometric standard star per night. However, changing weather conditions did not allow for absolute flux calibration and we therefore scaled the fluxes to match the observed PS1 *r*-band magnitudes. The spectra were not corrected for telluric absorption features.

7. The PS-ELQS Quasar Catalog

We conducted spectroscopic follow-up observations for 290 of our 334 good PS-ELQS candidates. We discovered a total of 218 new quasars, of which 190 are at $z \geq 2.8$. The resulting PS-ELQS quasar catalog includes a total of 592 quasars at $z \geq 2.8$:

1. 285 quasars from DR14Q
2. 190 newly discovered quasars (PS-ELQS)
3. 54 quasars from ELQS
4. 47 quasars from MQC
5. 13 quasars from J. Yang et al. (2019, in preparation)
6. three quasars from DR7Q.

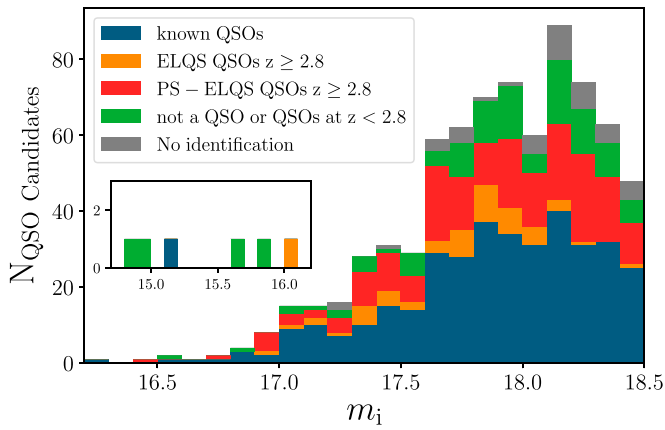


Figure 6. Histogram of the spectroscopic completeness of all good PS-ELQS candidates as a function of their dereddened PS1 i -band magnitude m_i . Dark blue and orange colors indicate all candidates from the general literature and the ELQS survey at $z \geq 2.8$. All newly identified candidates in this work are highlighted in red (QSOs at $z \geq 2.8$) and green (QSOs at $z < 2.8$ or not a QSO). All candidates that remain unidentified are depicted in gray.

Excluding the 40 candidates with unreliable photometry we could identify 592 quasars at $z \geq 2.8$ out of 766 good candidates ($=806-40$), of which 44 have not been observed. Therefore we calculate a minimum selection efficiency 77% ($592/766$) for the PS-ELQS quasar selection. For quasars at all redshifts our selection efficiency reaches $\sim 85\%$ ($650/766$). Out of the 72 objects which were identified not to be quasars at $z \geq 2.8$, we classified 36 as stars (K: 18, M: seven, G: two, F: two, one cataclysmic variable, and six unidentified stars) and 14 as galaxies. The remaining 22 objects are not quasars at $z \geq 2.8$, but have often too low S/N to classify them with certainty as a star, galaxy, or low-redshift quasar. The random forest classification results on the validation set (see Figure 3) suggest a much higher efficiency of 99% for quasars at any redshift. The discrepancy with the much lower observed efficiency of 85% is likely to originate in differences between the training set and the photometric sample. As we do not apply the *JKW2* color cut to the stars’ training set, because it results in an undersized sample size (314 objects), the distribution of stellar types in the training set is different from the photometric candidate sample. For example, 42% of stars in the training set are K and M stars, while this ratio increases to 69% once the *JKW2* color cut is applied to the training set. Therefore, the photometric candidate sample has likely a higher fraction of contaminants that can mimic quasars at $z > 2.8$, decreasing our overall efficiency.

The full PS-ELQS quasar catalog is published alongside this work in digital form. It also includes information on matches to *Galaxy Evolution Explorer* (*GALEX*), *ROSAT* 2RXS, and XMMSL2 (see Section 7.3 for details). Table 7 in Appendix A provides an overview over all the columns.

Figure 6 shows a histogram of all good candidates in the PS-ELQS sample as a function of their dereddened PS1 i -band magnitude, m_i . Known quasars at $z \geq 2.8$ in the literature are colored dark blue, excluding the known objects published as part of the ELQS (orange). All 190 newly identified quasars at $z \geq 2.8$ are shown in red, while all lower-redshift quasars and non-quasars are shown in green. The remaining 44 good candidates are highlighted in gray.

We present the discovery spectra of all newly identified quasars at $z \geq 2.8$ in Figures 9–11 in Appendix B. Additional

identification spectra for new lower-redshift quasars are shown in Figure 12. All discovery spectra are sorted by redshift, beginning with the lowest-redshift spectrum. A dark blue, orange, and red colored bar at the top of each spectrum indicates the broad Ly α , Si IV and C IV emission lines at 1215, 1400, 1549 Å (rest-frame). Strong artifacts, like cosmic rays, are removed using an iterative sigma-clipping procedure. The spectra are not smoothed and spectral fluxes are scaled according to the PS1 r -band photometric measurement. Redshifts for all newly discovered quasars are measured by visual comparison to a redshifted quasar template spectrum (Vanden Berk et al. 2001). We estimate this method to have a redshift uncertainty of $\Delta z \approx 0.02$.

We calculate absolute magnitudes at 1450 Å rest-frame, M_{1450} , from the dereddened PS1 i -band magnitudes for all quasars. This transformation includes a k -correction term which we estimate using a large grid of simulated quasar spectra. The simulated quasar spectra and synthetic PS1 magnitudes are generated by the `simqso`⁹ package (McGreer et al. 2013). The code begins by building a quasar continuum from a number of specified power-law slopes. Broad and narrow emission lines are then added onto the continuum as well as Fe emission and an IGM absorption model for the Ly α -forest. Our model does not account for intrinsic extinction from the quasar host galaxy, as the survey is targeted at the unobscured UV-bright quasar population. We adopt the values of Schindler et al. (2018) to build the spectral model and calculate a large grid of quasars with 28 cells over $m_i = 14-18$ and 53 cells across $z = 0.2-5.5$ with a total of 200 model spectra per cell. K -corrections are then calculated for each grid cell and interpolated to retrieve individual k -corrections for all newly identified quasars.

Figure 7 shows all 592 quasars of the PS-ELQS quasar catalog as a function of their absolute magnitudes, M_{1450} , and redshifts, z . Known quasars from the literature are divided into objects from the SDSS quasar catalogs (dark blue dots), sources from the MQC and J. Yang et al. (2019, in preparation, green triangles), and the ELQS quasar catalog (orange circles). Newly discovered quasars identified with this work are highlighted as red diamonds. The black solid line shows the faint-end magnitude limit of $m_i = 18.5$ converted into M_{1450} . Histograms depict the distributions along each axis.

We provide a list of all newly discovered quasars within the PS-ELQS quasar catalog ($z \geq 2.8$) in Table 8 in Appendix B. It contains the position in equatorial coordinates, the PS1 i -band magnitude, the absolute magnitude at 1450 Å, the determined spectroscopic redshift, near- and far-UV magnitudes from *GALEX* GR 6/7, and further notes. We provide the same information for all newly discovered quasars at $z < 2.8$ in Table 9 in Appendix C.

7.1. Quasar Discoveries at Low Declinations

The PS1 3π survey covers 3π sr of the northern sky, including the entire SDSS footprint. Therefore the PS-ELQS extends the efforts of the SDSS quasar surveys to a new region of ~ 9600 deg². The majority of that area (~ 5600 deg²) is at lower declinations (decl. = 30–0). The PS-ELQS quasar catalog contains 207 quasars at lower declinations, of which only 70 were known before. Therefore we approximately treble the known population of luminous intermediate-redshift quasars in this region.

⁹ <https://github.com/imcgreer/simqso>

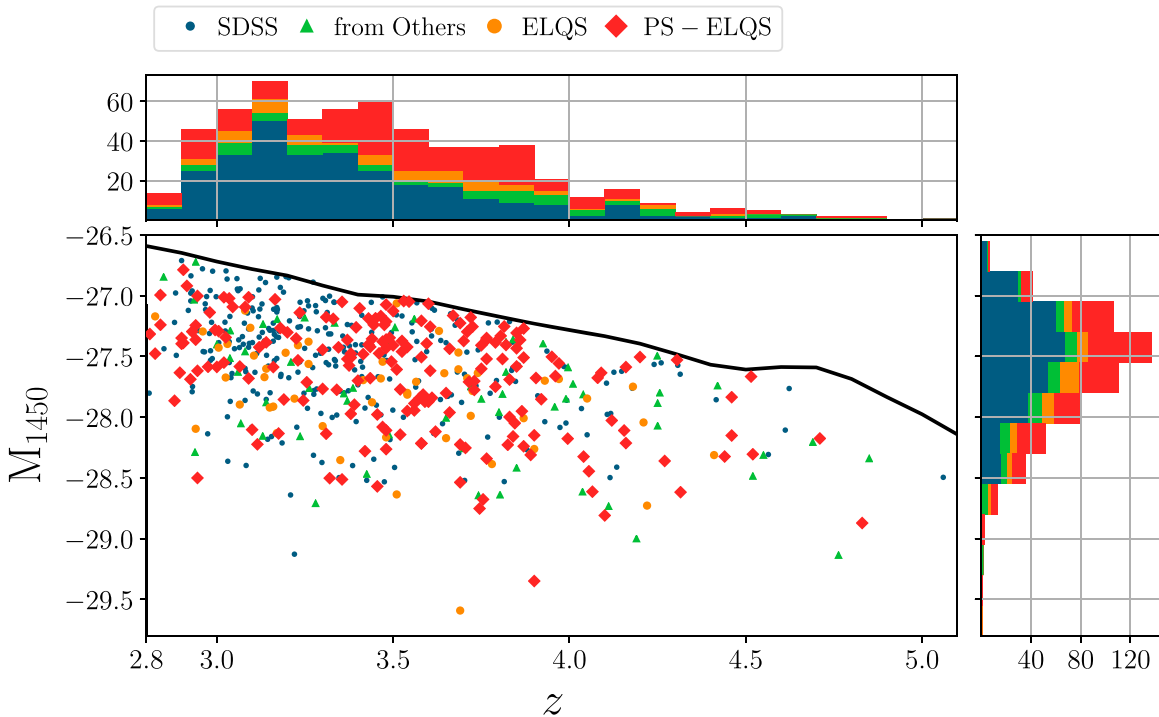


Figure 7. All quasars in the PS-ELQS quasar catalog in the absolute magnitude (M_{1450}) and redshift (z) plane. Quasars identified in the literature are shown as dark blue dots (SDSS DR7Q/DR14Q), green triangles (other sources), and small orange circles (ELQS). Newly identified quasars by the PS-ELQS are depicted as larger red diamonds. The solid black line shows our limit on the apparent PS1 i -band magnitude ($m_i = 18.5$). The histograms summarize the distribution of sources along their respective axis.

7.2. Notes on Broad Absorption Line Quasars

As part of the PS-ELQS we discovered a range of broad absorption line (BAL) quasars. Some of these objects have low-ionization BALs (LoBALs), showing broad absorption troughs from Mg II, and some of them also show absorption from meta-stable Fe II (FeLoBALs). We provide notes on the redshift identification and the absorption properties for some BAL quasars below, where the redshift measurement from the broad emission lines is difficult due to the absorption features. This is not an exhaustive list of all PS-ELQS quasars with BAL absorption features.

7.2.1. J003856.98–292224.3

This quasar is likely a FeLoBAL at $z \approx 2.27 \pm 0.005$ with strong nitrogen emission. The peak at $\sim 4150 \text{ \AA}$ is N V in the observed frame and the narrower line at 5750 \AA is N III] at 1750 \AA rest-frame. BAL troughs are seen in N V, C II, Si IV, C IV, Al II, Al III, and Fe II.

7.2.2. J021119.80–195943.0

J021119.80–195943.0 is a FeLoBAL at $z = 2.45 \pm 0.02$. The emission redshift is uncertain, because even the 1900 \AA complex is affected by absorption. It also displays unusually strong N III] 1750 \AA emission. The red edges of the troughs are around $z = 2.365$.

7.2.3. J023500.45+023829.2

This BAL quasars has a redshift of $z = 1.975 \pm 0.005$, primarily identified by the 1900 \AA complex. There is a C IV mini-BAL at $z = 1.96$ and a C IV BAL at $z = 1.85$.

7.2.4. J033559.99–132601.8

This LoBAL can be identified to be at $z = 1.900 \pm 0.005$ from the narrow C IV and Al III emission. It displays absorption in C IV, Al III, and Mg II.

7.2.5. J044756.84–230748.3

Based on multiple absorption lines arising from a nearby damped Ly α absorber, this quasar has a redshift of at least $z = 2.945 \pm 0.005$. It displays weak broad C IV emission from $5700\text{--}6300 \text{ \AA}$ and weak broad 1900 \AA emission around $7100\text{--}7600 \text{ \AA}$. It has a LoBAL with Si IV, C IV, and Al III at $z = 2.82$ as well as a mini-BAL in N V, Si IV, and C IV at $z = 2.745$.

7.2.6. J113252.86–063243.3

J113252.86–063243.3 is likely at $z = 2.41 \pm 0.01$, mainly identified from the 1900 \AA emission complex. It displays a LoBAL (Si IV, C IV, Al II, Al III) at $z = 2.27$. It further has narrower absorption troughs (Si IV, C IV, Al II, Al III) at $z = 2.319$, $z = 2.333$, and $z = 2.363$.

7.2.7. J191946.08+743747.1

This BAL quasar is at $z = 1.604 \pm 0.001$ identified by the narrow Mg II emission. It shows a FeLoBAL with Al II, Al III, Fe III, Fe II, and Mg II absorption. The red end of the troughs is around $z = 1.55$. It further displays narrow absorption in Al II, Al III, Fe II, and Mg II at $z = 1.5915 \pm 0.0005$.

7.2.8. J220912.01+061920.1

This quasar is at $z = 1.91 \pm 0.01$, identified by the narrow C IV and Al III lines. It displays a FeLoBAL (Si IV, C IV, Al II, Al III, Fe III, Mg II), where the blue end of the troughs is around

$z = 1.76$. It further has narrower Si IV, C IV, Al II, Al III, and Fe II absorption around $z = 1.893$.

7.3. Cross-matches to GALEX, ROSAT 2RXS, and XMMSL2

To obtain near- and far-UV photometry, we cross-matched the PS-ELQS quasar catalog with the *GALEX* GR6/7 Data Release (Martin et al. 2005) within $2''0$. We obtained the available photometry in the far- and near-UV bands at 1350–1750 Å and 1750–2750 Å, respectively.

We could identify a total of 49 matches to the full PS-ELQS catalog, of which 17 were detections in both bands, three only in the far-UV band, and 29 only in the near-UV band. Of all 190 newly discovered quasars four have detections in both *GALEX* bands and another seven are detected in the near-UV. The detections could potentially signal that the quasars' flux has not been fully absorbed by neutral hydrogen along the line of sight and thus these objects are likely promising targets for studies of He-reionization (e.g., Worseck et al. 2016).

In addition, we utilize the AllWISE counterparts to X-ray detections (Salvato et al. 2018) from the *ROSAT* (Truemper 1982) reprocessed 2RXS catalog (Boller et al. 2016) and the XMM Newton Slew 2 Survey (XMMSL2) to match the PS-ELQS quasar catalog with X-ray sources. We have matched the AllWISE positions of our sources to the AllWISE positions of the counterpart catalogs within a $1''0$ aperture.

There are a total of 12 matches between PS-ELQS and *ROSAT* 2RXS and three between PS-ELQS and XMMSL2.

Of the newly discovered quasars, one, J124615.10+713923.6 at $z = 3.995$, has an X-ray counterpart in *ROSAT* 2RXS with $f_{0.1-2.4 \text{ keV}} = 2.26 \times 10^{-13} \text{ erg cm}^{-2} \text{ s}^{-1}$ at a distance of $62''7$. As the match distance implies, this AllWISE source is not the most probable match to the X-ray source (TRXS_match_flag = 2) with a $p_i \approx 0.24$ relative probability to be the correct counterpart to the X-ray source among all possible AllWISE candidates. While we wanted to report this here for completeness, we would also like to caution against blindly associating the X-ray flux with the quasar.

Another new PS-ELQS quasar, J095947.52–103437.7 ($z = 3.165$), has a counterpart in XMMSL2. We further want to report on an XMMSL2 counterpart for the quasar J171721.32+422428.3 ($z = 3.495$). The latter quasar was discovered during pilot observations of the ELQS (Schindler et al. 2018), but not selected to be in the ELQS quasar catalog. In both cases the AllWISE counterparts constitute the best match to the X-ray source and seem reliable. The counterpart to J095947.52–103437.7 has a $0.24 \times 10^{-12} \text{ erg cm}^{-2} \text{ s}^{-1}$ detection in the soft band and a flux of $0.67 \times 10^{-12} \text{ erg cm}^{-2} \text{ s}^{-1}$ in the total band. The X-ray counterpart to J171721.32+422428.3 was detected in the soft band with $0.94 \times 10^{-12} \text{ erg cm}^{-2} \text{ s}^{-1}$ and in the total band with $2.42 \times 10^{-12} \text{ erg cm}^{-2} \text{ s}^{-1}$.

Information on all *GALEX*, *ROSAT* 2RXS, and XMMSL2 matches is included in the full PS-ELQS quasar catalog (see Table 7 in Appendix A).

8. Discussion

8.1. PS-ELQS Completeness Estimates

The goal of the PS-ELQS was to extend the novel quasar selection method of the ELQS to a much larger area. However, the final PS-ELQS quasar catalog includes only 343 quasars with $m_i \leq 18.0$ at $z \geq 2.8$ compared to the 407 quasars in the ELQS quasar catalog. A further comparison to the DR14Q

showed that we only recover roughly 56% (71%, 89%) of the bright ($m_i \leq 18.0$) quasars at $z \geq 2.8$ ($z \geq 3.0$, $z \geq 3.5$), indicating that the PS-ELQS missed quasars at $z \leq 3.5$ compared to the ELQS.

In order to understand this difference and characterize the biases in our selection we calculated the PS-ELQS completeness for the random forest classification and redshift estimation. The selection function is estimated based on the sample of simulated quasars that were used to determine the k -correction described in Section 7.

The PS-ELQS completeness of the quasar selection based on the random forest classification is shown in panel (a) of Figure 8. The results are generally independent of the i -band magnitude, but show clear features as a function of redshift. There are two redshift ranges, $z \approx 3.2\text{--}3.5$ and $z \approx 3.7\text{--}4.0$, where the completeness drops to 75%–85%. In the absence of u -band photometry these redshift ranges can be associated with stellar confusion. At $z \geq 5$ our completeness drops steeply, analogous to ELQS2. The absence of quasars at these redshifts and magnitudes in the training set results in incorrect classifications.

Panel (b) of Figure 8 shows the selection function resulting from the redshift selection based on the random forest regression (photometric redshift estimation). While we should select all quasars with $z_{\text{reg}} \geq 2.8$, we miss the majority (>50%) of sources between $z = 2.8$ and $z = 3.5$. This effect clearly explains why the PS-ELQS missed many known quasars at $z \leq 3.5$, which were selected by the original ELQS.

As the main difference of the PS-ELQS to the ELQS is the optical photometry, we suspect that our decreased completeness at lower redshifts is a result of the missing u -band photometry in PS1. In order to test this, we add the SDSS u -band photometry to the number of features for the random forest and rerun our completeness calculation. The selection functions for the re-run classification and redshift selections are displayed in panels (c) and (d) of Figure 8. The results clearly confirm our suspicion. Comparing panels (a) and (c) highlights how adding the u -band visibly improves the classification selection at $z \approx 3.2\text{--}3.5$ and $z \approx 3.7\text{--}4.0$. Furthermore, panels (b) and (d) emphasize that the missing u -band in PS1 is the cause of the low completeness at $z \leq 3.5$ for PS-ELQS. A second look at the comparison between photometric redshifts and spectroscopic values in Figure 4 shows that the quasars at $z \geq 2.5$ are predominantly found below the $z_{\text{spec}} = z_{\text{reg}}$ diagonal line. This translates into a bias on our photometric redshift estimates toward lower values, which in turn causes the low completeness in the redshift selection between $z = 2.8$ and $z = 3.5$.

8.2. Applications for the PS-ELQS Quasar Sample

In spite of the shortcomings of the PS-ELQS selection due to the missing u -band photometry of PS1, the PS-ELQS provides the most complete sample of extremely luminous quasars at $z = 3.5\text{--}5.0$. Our survey covered around $21,486 \text{ deg}^2$, making it the largest homogeneous spectroscopic quasar survey at these redshifts. We have successfully discovered 190 new quasars at $z \geq 2.8$, tripling the known quasars at decl. ≤ 0 in the PS-ELQS quasar catalog.

Our area coverage and the high completeness at $z = 3.5\text{--}5.0$ makes the PS-ELQS quasar sample uniquely equipped to constrain the volume density of extremely luminous quasars at intermediate redshifts. This is our first science goal, once the remaining 44 quasar candidates are observed to guarantee spectroscopic completeness.

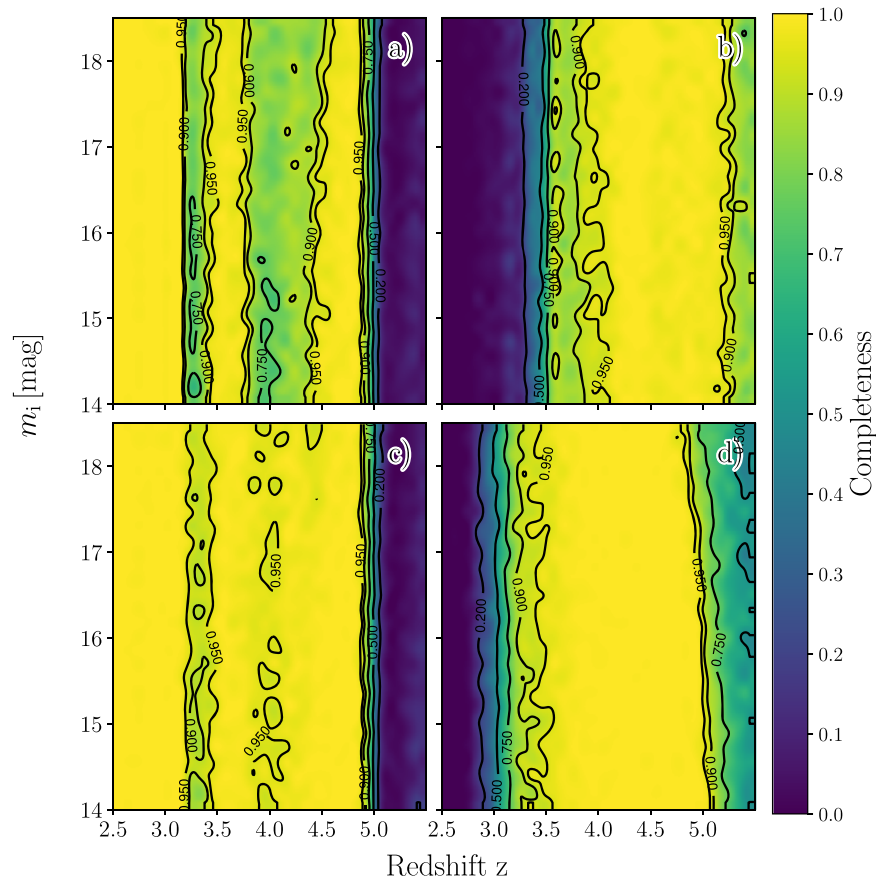


Figure 8. PS-ELQS completeness estimates as a function of redshift and i -band magnitude. The completeness maps were determined by the fraction of simulated quasars, selected by our different criteria, to all simulated quasars. Panel (a): Completeness of the PS-ELQS classification selection; panel (b): completeness of the PS-ELQS photometric redshift selection; panel (c): completeness of the classification selection (including the SDSS u -band); panel (d): completeness of the photometric redshift selection (including the SDSS u -band). Contour levels are drawn with solid lines at 20%, 50%, 75%, 90%, and 95% completeness.

Table 6
Possible Quasar Associations Identified from the PS-ELQS Sample

AllWISE Designation	R.A. (J2000) (hh:mm:ss.sss)	Decl. (J2000) (dd:mm:ss.ss)	z	Separation Angle (arcmin)	Proper 3D Distance (h^{-1} Mpc)
J030341.04–002321.8	03:03:41.045	–00:23:21.87	3.227
J030449.85–000813.4	03:04:49.859	–00:08:13.54	3.295	22.92	12.30
J091647.60–113009.9	09:16:47.616	–11:30:09.91	3.870
J091746.54–115331.9	09:17:46.542	–11:53:31.89	3.920	27.46	9.63
J102000.80–121151.4	10:20:00.800	–12:11:51.45	3.715
J102126.15–115621.4	10:21:26.131	–11:56:22.39	3.670	25.98	9.30
J172237.85+385951.9	17:22:37.854	+38:59:51.87	3.359
J172338.84+392621.4	17:23:38.809	+39:26:21.38	3.465	29.00	16.84
J235054.64+200938.6	23:50:54.634	+20:09:38.62	3.170
J235201.30+200902.3	23:52:01.307	+20:09:02.47	3.087	15.66	13.70
J230432.31–124819.6	23:04:32.312	–12:48:19.64	3.850
J230827.04–133256.2	23:08:27.042	–13:32:56.21	3.830	72.49	21.57
J230959.29–122603.2	23:09:59.293	–12:26:03.16	3.730	82.82	27.54

Four of our newly discovered quasars at $z = 2.900$, 2.905 , 2.905 , and 3.320 have far- and near-UV fluxes as measured by *GALEX*. We have visually confirmed these detections in *GALEX* photometry. These objects provide promising targets to investigate the He reionization of the universe. In general, the PS-ELQS quasars’ strong flux facilitates efficient

high-resolution spectroscopy to characterize the Ly α forest and intervening absorption systems.

From the PS-ELQS quasar catalog we have already identified five potential quasar pairs with angular separations of ≤ 30 arcmin and proper distances of $\leq 20 h^{-1}$ Mpc as well as an association of three quasars with larger angular distances but

similar redshifts. We provide details for all of these objects in Table 6. The relative distances are always measured with respect to the first object in the pair or association.

These quasar associations demonstrate the value of the PS-ELQS sample for quasar clustering measurements. Previous measurements on quasar clustering (e.g., Myers et al. 2006, 2007; Shen et al. 2007; da Ângela et al. 2008; Ross et al. 2009; White et al. 2012; Eftekharzadeh et al. 2015; Rodríguez-Torres et al. 2017; Timlin et al. 2018) have shown that these populations show a high level of clustering and that quasars are inferred to reside in dark matter haloes of $10^{12} h^{-1} M_{\odot}$ at most redshifts. Due to its size the PS-ELQS quasar sample will only allow for a very sparse measurement; however, the number of quasars should allow to constrain the minimum dark matter halo mass for this extremely luminous population at $z \sim 3.8$. In combination with the measurement of the ELQS quasar luminosity function (Schindler et al. 2019), one will be able to place constraints on the duty cycle of these rare objects.

9. Conclusions

We present the results of the PS-ELQS, a spectroscopic quasar survey covering $\sim 21,486 \text{ deg}^2$ of the 3π PS1 footprint. We apply the successful quasar selection strategy of the ELQS survey in the SDSS footprint to this larger area using the PS1 photometry. The candidates are selected based on a *JKW2* color cut using 2MASS *J* and *K_s*, and AllWISE *W2* photometry. Random forest photometric redshift estimation and classification on all Pan-STARRS PS1 and AllWISE *W1* and *W2* photometric bands lead to a highly efficient ($\geq 77\%$) quasar selection.

We selected a total of 806 bright ($m_i \leq 18.5$) quasar candidates with regression redshifts of $z_{\text{reg}} \geq 2.8$. After the exclusion of 428 sources known in the literature, of which 70 were identified with the ELQS survey, we rejected 40 candidates during visual inspection of their photometry.

We selected a total of 334 good candidates for spectroscopic follow-up observations and were able to observe 290 of the objects with the SOAR telescope, the MMT, and the VATT. We have discovered a total of 218 new quasars, of which 190 are at $z \geq 2.8$. Based on our quasar selection we have constructed the PS-ELQS quasar catalog with a total of 592 quasars, including the 190 newly discovered quasars at $z \geq 2.8$.

Estimates of the PS-ELQS completeness for the classification and photometric redshift selections show that the missing *u*-band photometry of PS1 lowers our completeness to select quasars at $z = 2.8\text{--}3.5$. This effect explains the low numbers of $z < 3.5$ quasars compared to the original ELQS selection. However, not accounting for the photometric completeness of PS1, the PS-ELQS general completeness at $z = 3.5\text{--}5.0$ is consistently above 70%. As a result, the PS-ELQS provides the most complete sample of extremely luminous quasars at $z = 3.5\text{--}5.0$.

A range of scientific applications will be able to leverage the information of this sample. For example, it is uniquely equipped to constrain the volume density of intermediate-redshift, extremely luminous quasars, to provide insight into quasar clustering of this rare population, and to facilitate studies of the IGM.

We would like to thank the anonymous referee for a thorough report with many supportive suggestions which helped to improve this paper.

J.-T.S., X.F., I.D.M., and J.Y. acknowledge support from NSF grant AST-1515115 and NASA ADAP grant NNX17AF28G.

K.C.L. acknowledges support from the U.S. National Science Foundation (NSF) under awards AST1715213 and AST-1312950 and through award SOSPA4-007 from the National Radio Astronomy Observatory (NRAO).

Based on observations obtained at the Southern Astrophysical Research (SOAR) telescope, which is a joint project of the Ministério da Ciência, Tecnologia, Inovações e Comunicações (MCTIC) do Brasil, the U.S. National Optical Astronomy Observatory (NOAO), the University of North Carolina at Chapel Hill (UNC), and Michigan State University (MSU).

Based on observations with the VATT: the Alice P. Lennon Telescope and the Thomas J. Bannan Astrophysics Facility.

Observations reported here were obtained at the MMT Observatory, a joint facility of the University of Arizona and the Smithsonian Institution.

This publication makes use of data products from the Two Micron All Sky Survey, which is a joint project of the University of Massachusetts and the Infrared Processing and Analysis Center/California Institute of Technology, funded by the National Aeronautics and Space Administration and the National Science Foundation.

This publication makes use of data products from the *Wide-field Infrared Survey Explorer*, which is a joint project of the University of California, Los Angeles, and the Jet Propulsion Laboratory/California Institute of Technology, funded by the National Aeronautics and Space Administration.

The Pan-STARRS1 Surveys (PS1) and the PS1 public science archive have been made possible through contributions by the Institute for Astronomy, the University of Hawaii, the Pan-STARRS Project Office, the Max Planck Society and its participating institutes, the Max Planck Institute for Astronomy, Heidelberg and the Max Planck Institute for Extraterrestrial Physics, Garching, The Johns Hopkins University, Durham University, the University of Edinburgh, the Queen's University Belfast, the Harvard-Smithsonian Center for Astrophysics, the Las Cumbres Observatory Global Telescope Network Incorporated, the National Central University of Taiwan, the Space Telescope Science Institute, the National Aeronautics and Space Administration under grant No. NNX08AR22G issued through the Planetary Science Division of the NASA Science Mission Directorate, the National Science Foundation grant No. AST-1238877, the University of Maryland, Eotvos Lorand University (ELTE), the Los Alamos National Laboratory, and the Gordon and Betty Moore Foundation.

Funding for the Sloan Digital Sky Survey IV has been provided by the Alfred P. Sloan Foundation, the U.S. Department of Energy Office of Science, and the Participating Institutions. SDSS acknowledges support and resources from the Center for High-Performance Computing at the University of Utah. The SDSS website is www.sdss.org.

SDSS is managed by the Astrophysical Research Consortium for the Participating Institutions of the SDSS Collaboration including the Brazilian Participation Group, the Carnegie Institution for Science, Carnegie Mellon University, the Chilean Participation Group, the French Participation Group, Harvard-Smithsonian Center for Astrophysics, Instituto de Astrofísica de Canarias, The Johns Hopkins University, Kavli Institute for the Physics and Mathematics of the Universe (IPMU)/University of Tokyo, Lawrence Berkeley National Laboratory, Leibniz Institut für Astrophysik Potsdam (AIP), Max-Planck-Institut für Astronomie (MPIA Heidelberg), Max-Planck-Institut für Astrophysik (MPA Garching), Max-Planck-Institut für Extraterrestrische

Physik (MPE), National Astronomical Observatories of China, New Mexico State University, New York University, University of Notre Dame, Observatório Nacional/MCTI, The Ohio State University, Pennsylvania State University, Shanghai Astronomical Observatory, United Kingdom Participation Group, Universidad Nacional Autónoma de México, University of Arizona, University of Colorado Boulder, University of Oxford, University of Portsmouth, University of Utah, University of Virginia, University of Washington, University of Wisconsin, Vanderbilt University, and Yale University.

This research has made use of the NASA/IPAC Extragalactic Database (NED) which is operated by the Jet Propulsion Laboratory, California Institute of Technology, under contract with the National Aeronautics and Space Administration.

This research made use of Astropy,¹⁰ a community-developed core Python package for Astronomy (Astropy Collaboration et al. 2013, 2018). In addition, python routines from scikit-learn (Pedregosa et al. 2011), SciPy (Jones et al. 2001), Matplotlib (Hunter 2007), and Pandas (McKinney 2011) were used in the quasar selection, data analysis and creation of the figures.

Appendix A The PS-ELQS Quasar Catalog

The PS-ELQS quasar catalog is available as a machine-readable table online. It has 56 columns, detailed in Table 7.

Table 7
Description of the Full PS-ELQS Quasar Catalog Table

Column	Column Name	Unit	Description
1	WISE	...	WISE AllWISE survey designation
2	PS1-RAdeg	deg	PS1 R.A., decimal degrees (J2000)
3	PS1-DEdeg	deg	PS1 Decl., decimal degrees (J2000)
4	PS1-RAh	h	PS1 Hour of R.A. (J2000)
5	PS1-RAm	m	PS1 Minute of R.A. (J2000)
6	PS1-RAs	s	PS1 Second of R.A. (J2000)
7	PS1-DE-	...	PS1 Sign of the Decl. (J2000)
8	PS1-DEd	deg	PS1 Degree of Decl. (J2000)
9	PS1-DEm	arcmin	PS1 Arcminute of Decl. (J2000)
10	PS1-DEs	arcsec	PS1 Arcsecond of Decl. (J2000)
11	ALLWISE-RAdeg	deg	ALLWISE R.A., decimal degrees (J2000)
12	ALLWISE-DEdeg	deg	ALLWISE Decl., decimal degrees (J2000)
13	Ref	...	Reference of the quasar classification
14	z-Ref	...	Best redshift of the quasar according to the reference
15	M1450	mag	Absolute magnitude at 1450Å calculated using the k-correction determined for this work
16-25	[band]mag-[survey]	mag	Dereddened AB magnitudes of the PS1 grizy, 2MASS jh k _s , and WISE W1W2 bands (surveys = [PS,2M,WISE]; bands = [g,r,i,z,y],[J,H,K],[W1,W2]).
26-35	e_[band]mag-[survey]	mag	1σ uncertainties on the AB magnitudes.
36	EBV	mag	E(B-V) color excess
37	GALEX-Match	Boolean to indicate successful matches with GALEX GR6/7
38	GALEX-Dist	arcsec	Match distance, GALEX GR6/7 to PS1 DR1
39	GALEX-NUVmag	mag	GALEX near-UV flux in magnitudes
40	e_GALEX-NUVmag	mag	Error on the GALEX near-UV flux
41	GALEX-FUVmag	mag	GALEX far-UV flux in magnitudes
42	e_GALEX-FUVmag	mag	Error on the GALEX far-UV flux
43	TRXS-match	...	Boolean to indicate successful matches to the ROSAT 2RXS AllWISE counterparts
44	TRXS-Dist	arcsec	Match distance between the ELQS AllWISE position to the ROSAT 2RXS AllWISE position. The distance values are often 0 or otherwise extremely small, because the positions match to numerical accuracy.
45	f_TRXS-match	...	A flag indicating the most probable AllWISE ROSAT 2RXS cross-match with 1. This is the case for all matched objects.
46	TRXS-FLUX	erg cm ⁻² s ⁻¹	2RXS flux
47	e_TRXS-FLUX	erg cm ⁻² s ⁻¹	2RXS flux error
48	XMM-match	...	Boolean to indicate successful matches to the XMMSL2 AllWISE counterparts
49	XMM-Dist	arcsec	Match distance between the ELQS AllWISE position to the XMMSL2 AllWISE counterparts
50	f_XMM-match	...	A flag indicating the most probable AllWISE XMMSL2 cross-match with 1. This is the case for all matched objects.
51	XMM-FLUX-B8	10 ⁻¹² erg cm ⁻² s ⁻¹	Total band (0.2–12.0 keV) flux
52	XMM-FLUX-B7	10 ⁻¹² erg cm ⁻² s ⁻¹	Hard band (2.0–12.0 keV) flux
53	XMM-FLUX-B6	10 ⁻¹² erg cm ⁻² s ⁻¹	Soft band (0.2–2.0 keV) flux
54	e_XMM-FLUX-B8	10 ⁻¹² erg cm ⁻² s ⁻¹	Total band (0.2–12.0 keV) flux error
55	e_XMM-FLUX-B7	10 ⁻¹² erg cm ⁻² s ⁻¹	Hard band (2.0–12.0 keV) flux error
56	e_XMM-FLUX-B6	10 ⁻¹² erg cm ⁻² s ⁻¹	Soft band (0.2–2.0 keV) flux error

(This table is available in its entirety in machine-readable form.)

¹⁰ <http://www.astropy.org>

Appendix B

Newly Discovered QSOs at $z \geq 2.8$

We present general properties of the 190 newly discovered PS-ELQS quasars in Table 8. Their discovery spectra are shown in Figures 9–11.

Table 8
Newly Discovered Quasars at $z \geq 2.8$ in the PS-ELQS Sample

R.A. (J2000) (hh:mm:ss.sss)	Decl. (J2000) (dd:mm:ss.ss)	m_i (mag)	M_{1450} (mag)	Spectroscopic Redshift	Near-UV ^a (mag)	Far-UV ^a (mag)	Notes ^b
00:20:27.082	-18:44:00.97	18.31 ± 0.01	-27.35	3.765	171008
00:27:25.651	-26:44:32.00	17.93 ± 0.01	-27.29	3.005	171008
00:43:46.841	-11:17:02.06	17.41 ± 0.00	-28.11	3.480	171007
00:55:15.845	-14:59:15.50	18.39 ± 0.01	-27.50	4.200	171008
01:02:48.769	-20:07:28.70	18.32 ± 0.01	-27.30	3.710	171010
01:03:05.501	-24:49:25.25	17.77 ± 0.01	-27.95	3.865	180122
01:03:18.075	-13:05:10.19	17.22 ± 0.00	-28.61	4.065	171007
01:09:33.398	+38:20:15.82	18.45 ± 0.01	-27.18	3.720	171020
01:18:52.261	-09:40:16.07	17.98 ± 0.00	-27.54	3.495	171008
01:28:18.883	-09:57:00.44	18.14 ± 0.01	-27.52	3.765	171008
01:29:48.978	-04:21:49.49	18.48 ± 0.00	-27.07	3.600	171010
01:39:11.231	-02:31:33.65	18.38 ± 0.01	-27.23	3.690	171010
01:40:46.361	+36:41:30.22	18.25 ± 0.02	-27.18	3.310	171021
01:50:41.591	-25:08:46.35	17.70 ± 0.01	-27.87	3.600	171008
01:51:06.839	-28:39:33.76	17.87 ± 0.00	-27.78	3.730	171007
02:01:58.777	+37:17:45.47	18.16 ± 0.01	-27.68	4.080	171020
02:08:25.254	+17:05:48.91	17.66 ± 0.01	-27.77	3.300	171010
02:12:20.417	+09:17:49.15	17.64 ± 0.01	-27.59	3.000	171008
02:14:21.635	+09:04:07.05	17.61 ± 0.01	-27.94	3.560	171009
02:19:48.831	+34:47:19.63	17.74 ± 0.01	-27.59	3.160	171020
02:21:23.915	-14:16:54.82	17.80 ± 0.01	-27.80	3.650	180124
02:21:26.889	-28:22:51.31	18.31 ± 0.01	-27.21	3.480	171008
02:23:25.100	+22:12:11.77	18.43 ± 0.01	-27.25	3.815	171021
02:28:40.587	+35:26:17.59	17.52 ± 0.01	-27.97	3.380	171020
02:31:49.748	-11:15:20.81	18.32 ± 0.00	-27.19	3.430	171010
02:35:51.443	-17:57:25.67	18.16 ± 0.00	-27.39	3.595	171009
02:45:26.449	+37:10:07.34	17.67 ± 0.01	-27.89	3.560	171111
02:49:32.661	+27:59:25.10	18.22 ± 0.01	-27.01	3.020	171116
02:55:29.671	+12:28:26.46	17.50 ± 0.01	-28.24	3.870	171010
02:57:21.095	+15:33:23.09	17.30 ± 0.01	-28.14	3.310	171010
03:01:51.627	+12:12:04.58	17.10 ± 0.00	-28.54	3.690	171010
03:05:17.924	-20:56:28.22	18.11 ± 0.01	-27.66	3.960	171007
03:05:59.775	+24:25:07.32	18.17 ± 0.01	-27.52	3.810	171109
03:25:09.436	+27:12:00.36	18.34 ± 0.01	-27.21	3.580	171111
03:29:06.257	+20:24:57.82	17.82 ± 0.01	-27.53	3.230	171111
03:31:36.931	+21:29:32.29	17.48 ± 0.01	-27.85	3.190	171109
03:39:08.180	-15:38:21.18	17.93 ± 0.00	-27.75	3.790	171006
03:41:18.143	+02:24:37.30	17.60 ± 0.01	-27.68	3.090	171008
03:53:14.885	-25:18:14.85	18.45 ± 0.01	-27.53	4.305	171008
03:55:50.316	-14:56:39.05	18.28 ± 0.01	-27.24	3.475	171010
03:56:17.616	-12:03:09.63	18.29 ± 0.00	-27.36	3.765	171008
03:58:11.141	+25:04:01.62	18.24 ± 0.01	-27.41	3.750	171111
03:59:15.718	-07:41:42.13	17.24 ± 0.00	-28.28	3.420	171006
03:59:22.959	-19:11:27.82	17.87 ± 0.01	-27.24	2.840	171009
04:08:20.966	-03:08:29.58	18.06 ± 0.00	-27.60	3.750	171009
04:09:14.876	-27:56:32.89	17.95 ± 0.00	-28.15	4.460	171006
04:10:53.654	-07:47:44.82	17.62 ± 0.00	-27.59	2.975	171009
04:11:02.077	-01:35:15.15	17.64 ± 0.01	-27.96	3.660	171006
04:32:29.308	-19:17:17.82	17.88 ± 0.00	-27.30	2.930	171009
04:41:32.015	-10:16:34.27	18.21 ± 0.01	-27.56	3.970	171008
04:47:56.843	-23:07:48.29	16.71 ± 0.00	-28.50	2.945	171006 ^c
04:53:16.580	-09:30:24.94	18.39 ± 0.00	-27.10	3.405	180124
04:54:20.311	-00:37:31.84	18.25 ± 0.02	-26.92	2.915	180124
04:59:50.110	+07:28:02.71	18.09 ± 0.01	-27.42	3.435	22.67 ± 0.32	...	180124
05:00:15.026	-24:39:27.24	17.92 ± 0.00	-27.61	3.510	171007
05:03:54.146	-06:08:25.04	18.22 ± 0.01	-27.02	3.035	180124

Table 8
(Continued)

R.A. (J2000) (hh:mm:ss.sss)	Decl. (J2000) (dd:mm:ss.ss)	m_i (mag)	M_{1450} (mag)	Spectroscopic Redshift	Near-UV ^a (mag)	Far-UV ^a (mag)	Notes ^b
05:20:01.728	-20:14:40.59	18.26 ± 0.00	-27.50	3.950	171008
05:21:36.923	-13:39:38.79	17.60 ± 0.00	-28.36	4.270	171006
05:39:46.870	-20:08:41.86	18.29 ± 0.01	-27.38	3.790	171021
08:18:24.472	+82:06:48.47	17.35 ± 0.01	-28.22	3.580	180517
08:51:03.208	+13:02:53.32	18.47 ± 0.01	-27.04	3.530	180122
09:16:47.616	-11:30:09.91	18.44 ± 0.01	-27.27	3.870	180122
09:17:46.542	-11:53:31.89	17.90 ± 0.01	-27.85	3.920	171111
09:19:23.109	-00:52:08.00	17.56 ± 0.00	-27.62	2.945	180122
09:28:05.302	+28:27:19.72	17.80 ± 0.01	-27.70	3.400	21.48 ± 0.23	...	171109
09:34:04.053	-11:11:25.13	17.94 ± 0.01	-27.62	3.605	180122
09:35:42.696	-06:51:18.94	17.50 ± 0.01	-28.32	4.040	180122
09:40:24.121	-03:23:04.13	17.60 ± 0.00	-28.15	3.900	180123
09:50:34.733	-21:02:50.74	18.16 ± 0.01	-27.36	3.480	180124
09:59:47.524	-10:34:37.50	18.28 ± 0.03	-27.03	3.165	21.81 ± 0.28	...	180123
10:14:30.281	-04:21:40.32	17.44 ± 0.01	-28.31	3.890	180123
10:15:29.367	-12:13:14.34	17.06 ± 0.00	-28.81	4.100	180123
10:15:40.799	-03:27:47.25	17.67 ± 0.01	-28.05	3.845	180123
10:15:44.118	-11:09:22.77	17.56 ± 0.00	-28.16	3.840	180123
10:20:00.800	-12:11:51.45	17.92 ± 0.01	-27.71	3.715	180404
10:21:26.131	-11:56:22.39	18.43 ± 0.01	-27.16	3.670	180405
10:31:58.288	-21:44:07.40	17.69 ± 0.00	-27.87	3.590	180404
10:41:38.997	-09:44:37.94	18.22 ± 0.02	-27.14	3.235	180321
10:46:27.942	-23:39:17.54	18.04 ± 0.01	-27.51	3.580	180122
10:47:13.545	-06:45:38.19	18.42 ± 0.01	-27.05	3.355	180405
10:51:22.689	-06:50:47.84	17.34 ± 0.01	-28.34	3.765	180122
10:53:53.499	+25:31:15.50	18.39 ± 0.01	-27.13	3.500	180321
10:54:49.678	-17:11:07.39	16.92 ± 0.00	-28.75	3.745	20.68 ± 0.10	...	180122
11:08:48.484	-10:22:07.31	18.26 ± 0.01	-27.84	4.460	180123
11:10:54.687	-30:11:29.95	17.38 ± 0.00	-28.87	4.830	180122 ^d
11:13:05.343	-21:25:40.65	17.60 ± 0.01	-27.90	3.390	180122
11:13:34.586	-07:50:33.49	18.15 ± 0.01	-27.09	3.045	180405
11:14:03.257	-05:02:35.09	17.48 ± 0.00	-28.23	3.825	180122
11:14:28.309	-04:09:38.76	18.27 ± 0.02	-27.24	3.445	180405
11:19:56.987	-19:28:32.42	18.01 ± 0.02	-27.69	3.830	180123
11:29:39.605	-23:33:49.64	17.28 ± 0.00	-27.86	2.880	180123
11:33:55.641	-23:05:24.38	18.15 ± 0.01	-27.44	3.660	180405
11:44:17.308	-05:45:34.69	18.11 ± 0.01	-27.41	3.500	180405
11:49:14.377	-15:30:43.93	17.68 ± 0.01	-28.21	4.160	180404
11:56:32.386	-07:21:14.26	18.37 ± 0.01	-26.79	2.905	21.70 ± 0.27	21.73 ± 0.49	180405
12:09:29.549	-05:17:37.06	18.43 ± 0.01	-27.07	3.480	180405
12:10:16.802	+80:56:03.21	18.17 ± 0.04	-27.35	3.490	180514
12:10:30.332	-09:57:25.39	18.03 ± 0.01	-27.30	3.200	180405
12:30:10.034	-06:33:34.10	17.97 ± 0.01	-27.44	3.300	180404
12:36:12.047	-11:36:00.62	18.00 ± 0.01	-27.35	3.225	180405
12:46:10.755	+75:17:11.07	17.40 ± 0.00	-28.14	3.520	180517
12:46:15.090	+71:39:23.60	17.62 ± 0.00	-28.18	3.995	180517
12:58:50.976	-18:54:30.55	17.67 ± 0.00	-27.71	3.255	180124
13:00:31.133	-28:29:31.01	17.94 ± 0.00	-28.18	4.710	180124 ^d
13:01:48.270	-14:46:52.70	18.44 ± 0.02	-27.67	4.515	180124
13:02:30.435	-10:26:28.59	18.29 ± 0.01	-27.41	3.820	180124
13:05:00.904	-12:26:18.79	18.17 ± 0.01	-27.09	3.080	180405
13:16:44.039	-25:38:10.33	18.12 ± 0.01	-27.36	3.370	180405
13:17:25.036	-18:42:30.76	18.24 ± 0.01	-27.37	3.700	180404
13:29:56.958	-04:52:21.77	18.23 ± 0.02	-27.26	3.395	180406
13:39:32.277	+36:13:40.62	18.33 ± 0.01	-27.19	3.450	180321
13:58:32.274	-28:48:35.48	18.40 ± 0.02	-27.31	3.850	180602
14:00:15.152	-03:44:16.50	17.60 ± 0.01	-27.95	3.540	180404
14:08:01.817	-27:58:20.35	17.77 ± 0.01	-28.32	4.440	180404
14:11:42.768	-24:13:13.48	18.11 ± 0.01	-27.42	3.540	180404
14:27:32.247	-18:03:18.31	17.07 ± 0.02	-28.22	3.115	180404
14:32:54.468	-27:22:28.05	18.37 ± 0.02	-27.25	3.725	180602
14:39:49.242	-08:07:05.38	18.10 ± 0.01	-27.40	3.430	180602
14:45:49.741	-11:10:15.68	17.94 ± 0.00	-27.28	2.995	180404

Table 8
(Continued)

R.A. (J2000) (hh:mm:ss.sss)	Decl. (J2000) (dd:mm:ss.ss)	m_i (mag)	M_{1450} (mag)	Spectroscopic Redshift	Near-UV ^a (mag)	Far-UV ^a (mag)	Notes ^b
14:55:59.430	-25:28:32.10	18.28 ± 0.01	-27.59	4.160	180404
15:18:53.216	-11:59:51.54	17.83 ± 0.00	-27.68	3.435	180404
15:23:12.411	-16:27:22.92	17.83 ± 0.00	-28.03	4.120	180404
15:32:45.990	-25:10:48.22	17.78 ± 0.01	-28.11	4.155	180404
15:38:15.568	+81:44:32.99	18.06 ± 0.01	-27.27	3.180	21.43 ± 0.21	...	180514
15:49:16.840	-22:37:46.53	18.06 ± 0.01	-27.68	3.905	180405
15:56:35.483	+60:37:26.78	17.69 ± 0.00	-27.77	3.340	180517
15:58:41.854	-04:03:53.42	17.68 ± 0.01	-27.55	3.020	180405
16:00:19.482	-12:17:02.75	18.07 ± 0.01	-27.14	2.980	180405
16:01:11.971	-16:43:41.63	18.12 ± 0.01	-26.99	2.840	180602
16:06:08.999	+48:41:37.02	18.04 ± 0.01	-27.42	3.345	21.39 ± 0.15	...	180517
16:16:48.948	-09:14:44.39	17.39 ± 0.01	-28.45	4.055	180405
16:17:37.785	+59:50:20.13	17.39 ± 0.02	-28.62	4.315	180517
16:23:49.985	-15:44:27.68	17.81 ± 0.03	-27.35	2.900	180406
16:29:36.489	+60:40:49.19	17.93 ± 0.01	-27.24	2.940	180517
16:31:18.216	-12:43:08.60	16.96 ± 0.01	-28.57	3.455	180406
16:32:27.929	-14:20:44.18	17.00 ± 0.01	-28.68	3.755	180406
16:35:36.073	+03:24:07.80	16.95 ± 0.00	-28.50	3.320	20.54 ± 0.15	21.53 ± 0.35	180321
16:38:56.009	+69:18:15.24	18.02 ± 0.01	-27.48	3.415	180517
16:39:26.455	+03:52:04.12	17.52 ± 0.00	-27.86	3.245	180321
16:48:52.744	+09:59:42.10	17.77 ± 0.00	-27.39	2.905	20.80 ± 0.09	21.28 ± 0.12	180321
16:59:29.379	+65:38:20.85	18.35 ± 0.00	-27.33	3.805	180514
17:20:46.132	+00:43:28.19	17.91 ± 0.01	-27.57	3.375	180320
17:30:03.673	+48:46:30.77	16.97 ± 0.01	-28.51	3.355	180518
17:47:13.484	+29:55:32.30	18.34 ± 0.01	-27.17	3.465	180321
17:53:34.530	+37:49:07.13	18.19 ± 0.01	-27.00	2.945	180518
17:55:21.128	+30:09:04.24	17.89 ± 0.00	-27.34	3.025	180321
17:56:29.853	+26:07:40.57	17.27 ± 0.01	-28.26	3.480	180320
18:02:09.690	+40:12:53.77	18.16 ± 0.01	-27.37	3.525	180518
18:10:27.309	+34:24:08.85	18.26 ± 0.01	-27.19	3.330	171109
18:10:41.346	+34:54:49.46	18.04 ± 0.01	-27.47	3.460	171109
18:17:06.185	+48:22:26.07	17.39 ± 0.02	-28.25	3.705	180518
18:19:14.803	+33:39:45.98	17.74 ± 0.00	-27.84	3.610	171020
19:35:12.403	-26:10:49.63	17.20 ± 0.00	-28.13	3.175	171007
20:00:13.515	-25:05:36.92	17.72 ± 0.01	-27.84	3.575	171006
20:02:05.969	-23:28:26.52	17.82 ± 0.01	-27.36	2.940	171007
20:10:23.353	-18:23:47.75	18.15 ± 0.00	-27.36	3.440	171010
20:11:58.767	-26:23:40.95	17.47 ± 0.00	-28.12	3.620	171008
20:17:41.494	-28:16:29.96	17.40 ± 0.01	-28.22	3.690	171008
20:18:34.860	-15:28:38.69	17.35 ± 0.01	-28.22	3.580	171007
20:20:43.904	-02:37:02.52	17.75 ± 0.01	-27.81	3.585	171008
20:33:36.699	-24:56:15.86	18.14 ± 0.01	-27.38	3.470	171010
20:33:43.573	-30:23:09.83	17.76 ± 0.00	-27.77	3.520	171007
20:34:16.997	-02:59:53.43	18.26 ± 0.00	-27.01	3.090	180602
20:36:23.526	-08:37:29.92	17.51 ± 0.01	-27.63	2.895	171008
20:43:20.175	-03:38:40.93	17.48 ± 0.02	-27.69	2.925	171009
20:48:48.274	-22:51:52.15	17.18 ± 0.00	-28.10	3.100	171009
21:03:51.499	-26:23:00.22	17.54 ± 0.00	-27.98	3.455	171006
21:11:11.604	-25:36:15.03	17.96 ± 0.01	-27.52	3.370	171007
21:25:40.966	-17:19:51.41	16.42 ± 0.00	-29.35	3.900	171010
21:26:51.969	-10:31:39.62	18.21 ± 0.01	-27.51	3.870	171008
21:27:16.485	-04:04:33.58	18.47 ± 0.02	-27.05	3.545	171010
21:30:50.101	-24:44:03.50	18.01 ± 0.01	-27.48	3.380	171009
21:32:25.900	-28:31:33.33	17.76 ± 0.01	-27.32	2.810	171009
21:34:45.240	-27:49:39.75	17.68 ± 0.00	-27.58	3.065	22.89 ± 0.47	...	171009
22:21:52.882	-18:26:02.94	17.80 ± 0.01	-28.30	4.520	171010
22:29:59.998	-26:21:05.68	17.91 ± 0.01	-27.38	3.140	171008
22:30:49.477	-21:54:02.09	18.30 ± 0.01	-27.26	3.605	180602
22:37:34.408	-31:07:14.09	17.87 ± 0.01	-27.42	3.120	171009
22:46:19.167	-25:17:20.76	17.76 ± 0.01	-27.40	2.900	21.71 ± 0.27	22.55 ± 0.54	171007
22:56:33.174	-12:43:59.64	17.62 ± 0.01	-27.48	2.825	171009
22:58:20.943	-28:18:55.25	18.07 ± 0.01	-27.46	3.525	171009
22:59:39.043	-22:50:35.10	17.43 ± 0.01	-28.08	3.470	171007

Table 8
(Continued)

R.A. (J2000) (hh:mm:ss.sss)	Decl. (J2000) (dd:mm:ss.ss)	m_i (mag)	M_{1450} (mag)	Spectroscopic Redshift	Near-UV ^a (mag)	Far-UV ^a (mag)	Notes ^b
23:00:22.023	-14:40:31.37	18.28 ± 0.00	-27.43	3.850	171008
23:04:32.312	-12:48:19.64	18.13 ± 0.01	-27.58	3.850	171007
23:08:27.042	-13:32:56.21	17.71 ± 0.01	-28.00	3.830	171006
23:09:59.293	-12:26:03.16	17.94 ± 0.00	-27.70	3.730	171006
23:23:06.892	-24:51:13.78	18.35 ± 0.01	-27.36	3.860	171007
23:39:26.346	-11:20:50.35	18.20 ± 0.01	-27.64	4.090	171021
23:42:10.117	-23:21:53.60	18.09 ± 0.01	-27.43	3.480	171008
23:42:41.975	-12:26:55.02	17.98 ± 0.00	-27.51	3.380	171006

Notes.

^a The near and far-UV magnitudes were obtained from cross-matches within 2''0 to the *GALEX* GR6/7 data release.

^b This column shows the observation date (YYMMDD) and provides further information on individual objects.

^c This object has been classified as a BAL, LoBAL, or FeLoBAL quasar. Details are discussed in Section 7.2.

^d These objects were also independently discovered by Yang et al. (2019b).

(This table is available in machine-readable form.)

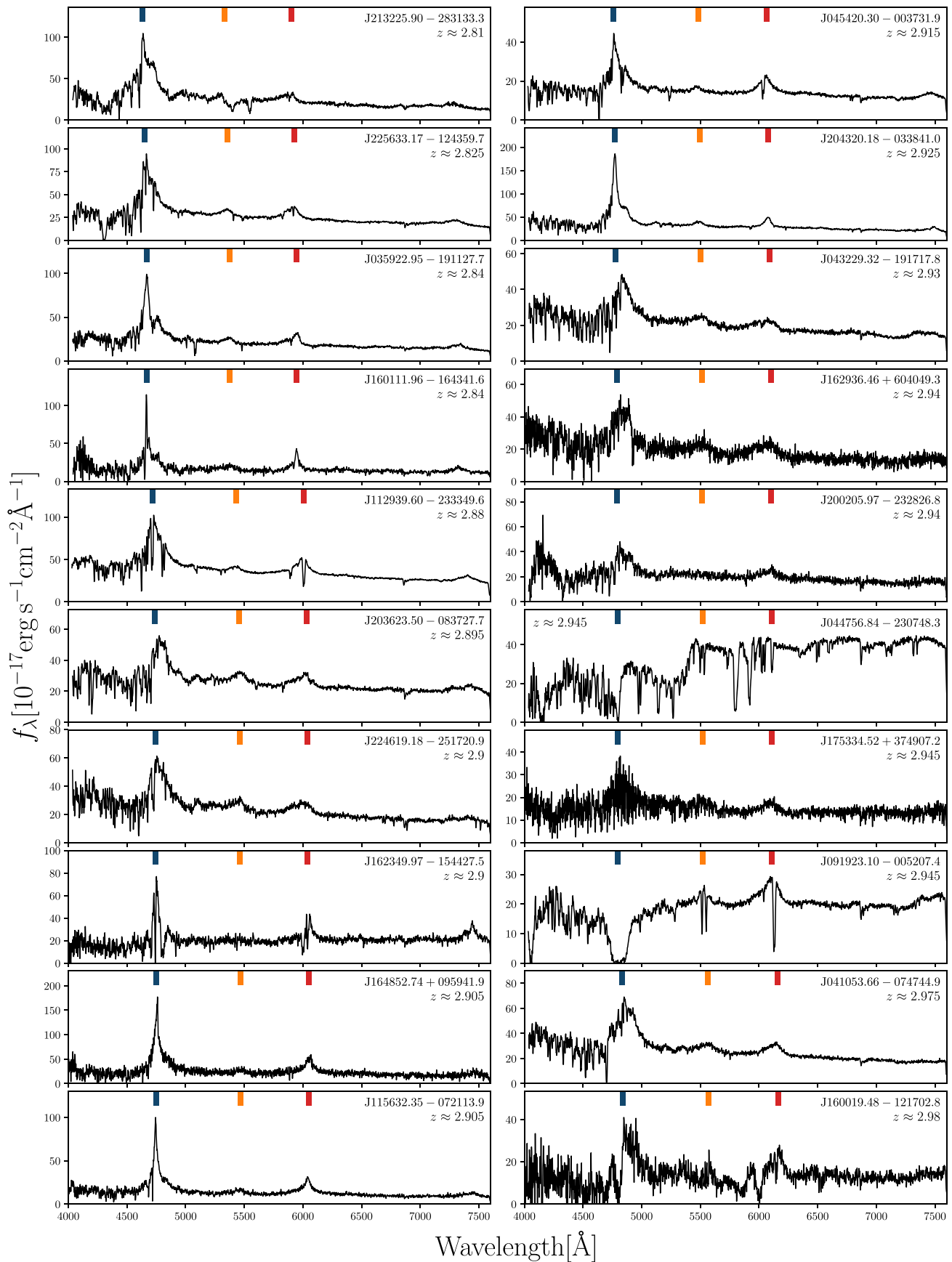


Figure 9. Discovery spectra of the newly discovered PS-ELQS quasars. The dark blue, orange, and red bars denote the center positions of the broad Ly α , Si IV, and C IV emission lines according to the spectroscopic redshift.

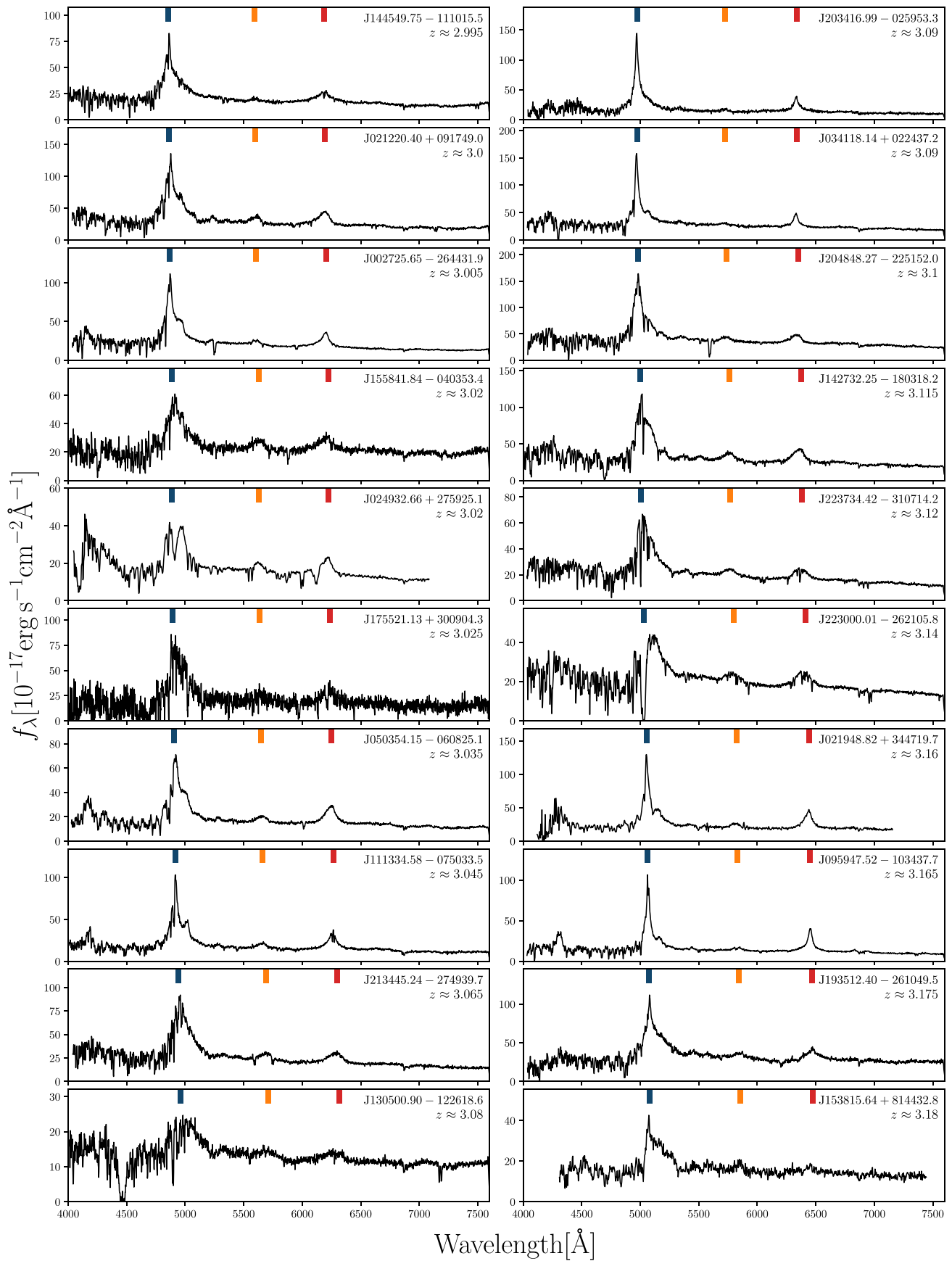


Figure 9. (Continued.)

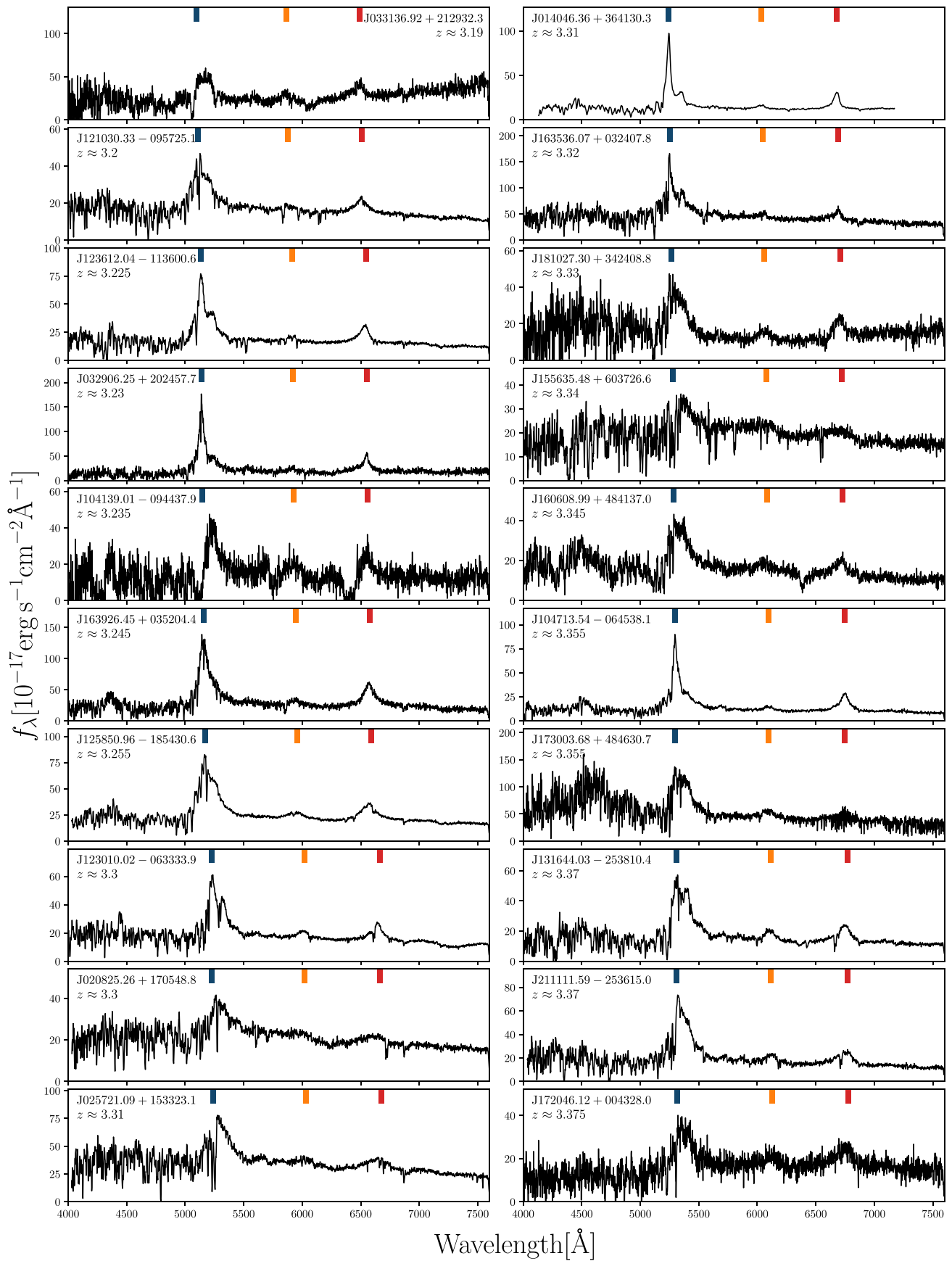


Figure 9. (Continued.)

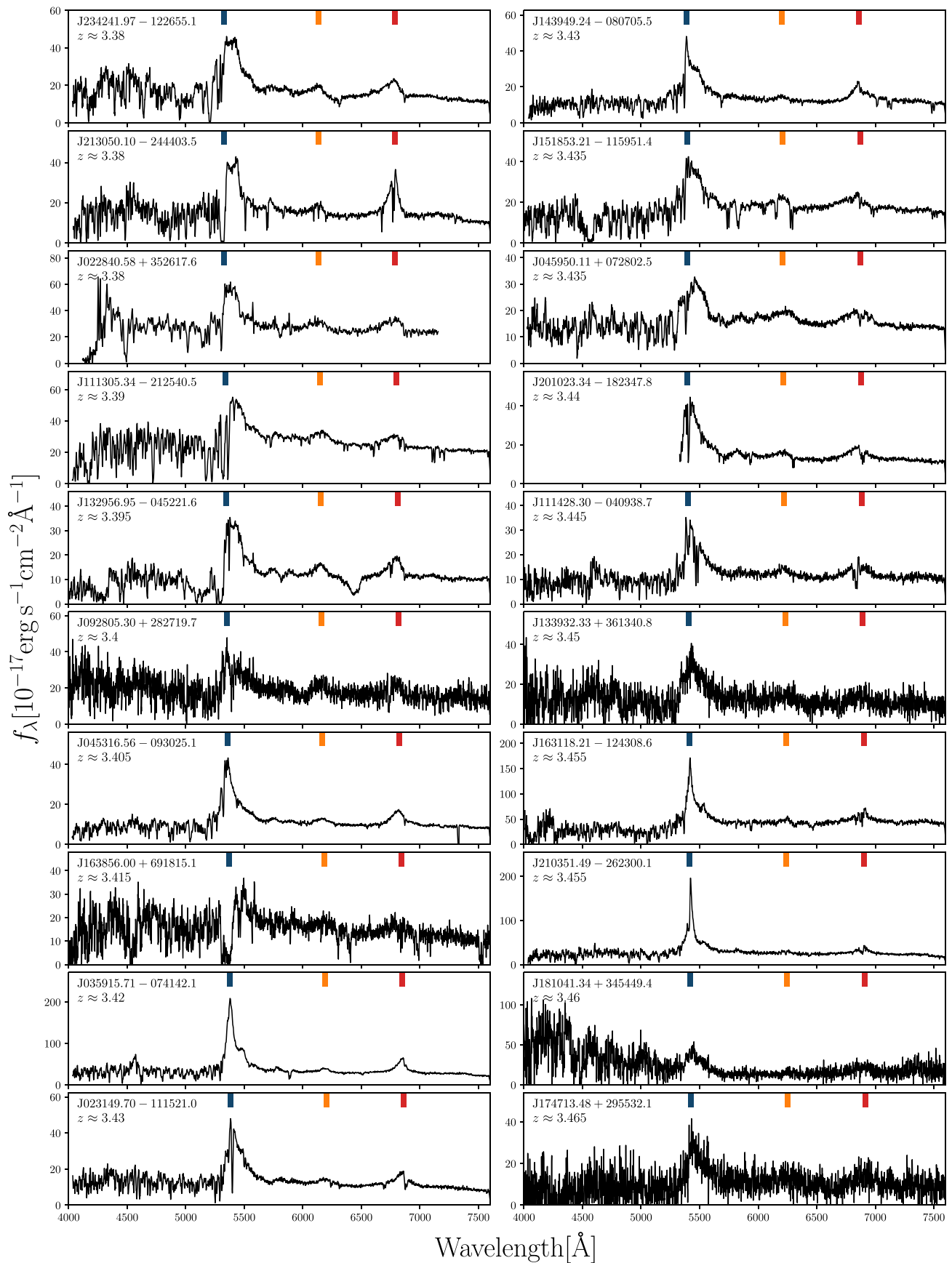


Figure 10. Discovery spectra of the newly discovered PS-ELQS quasars (continued).

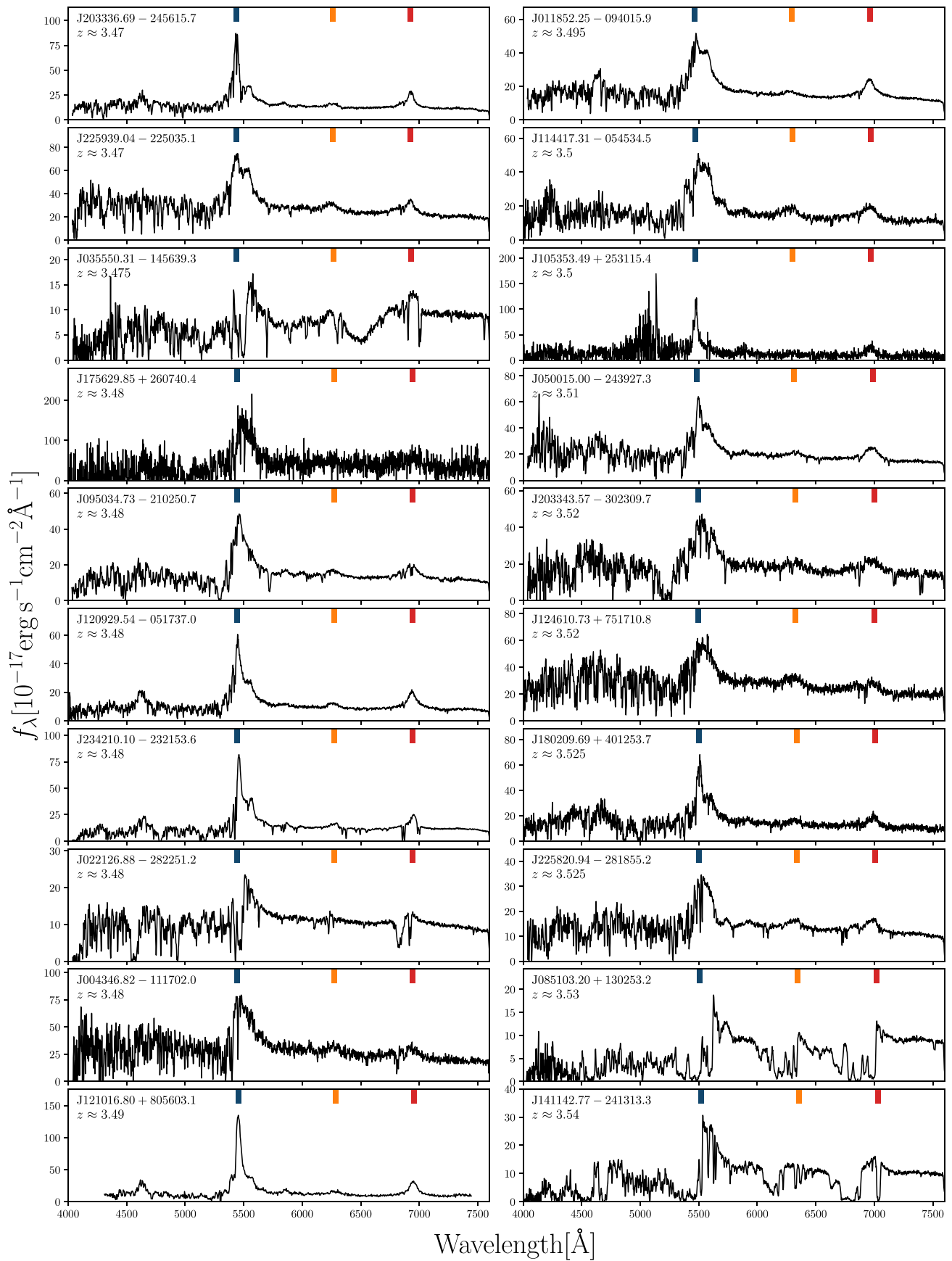


Figure 10. (Continued.)

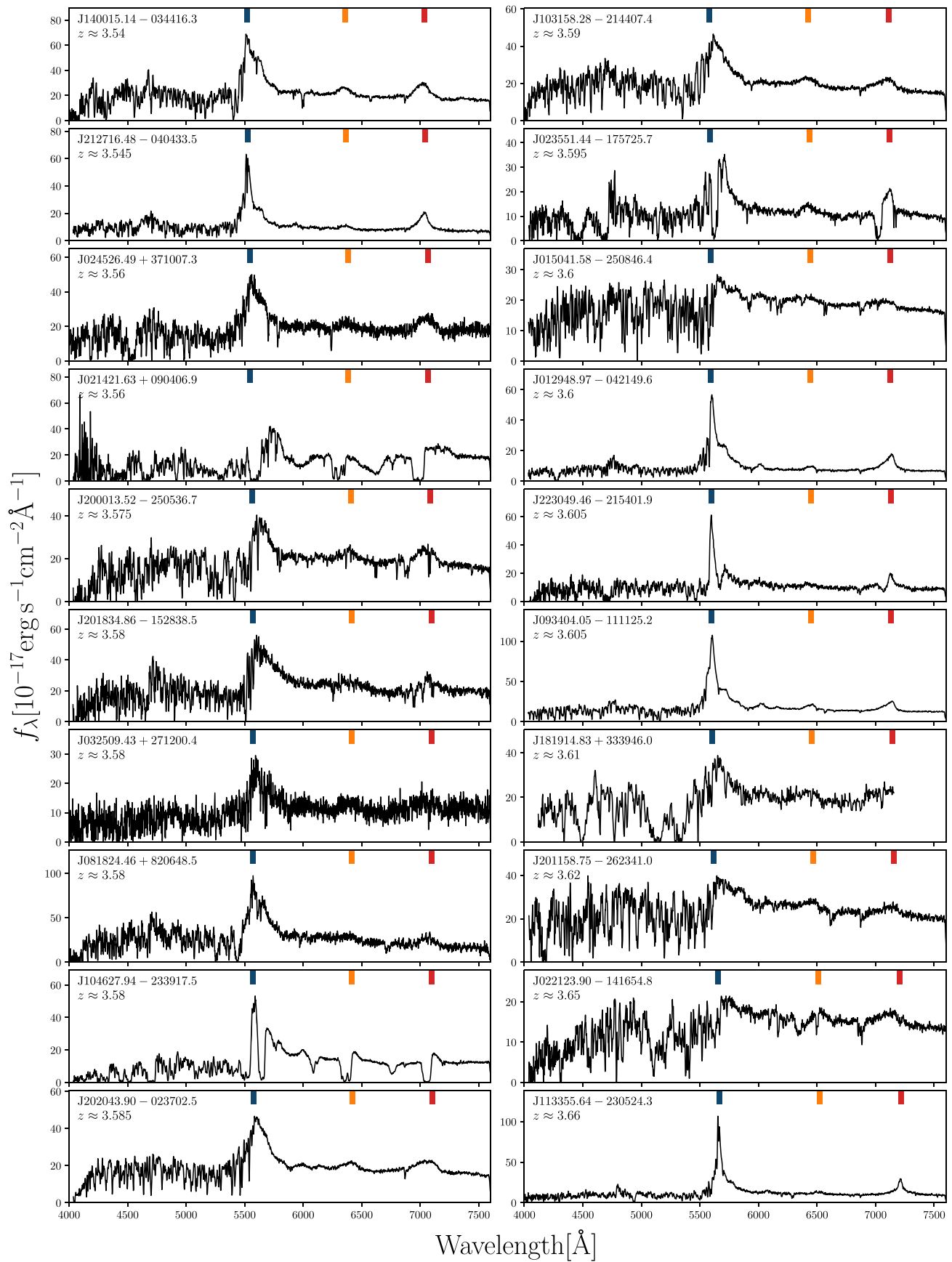


Figure 10. (Continued.)

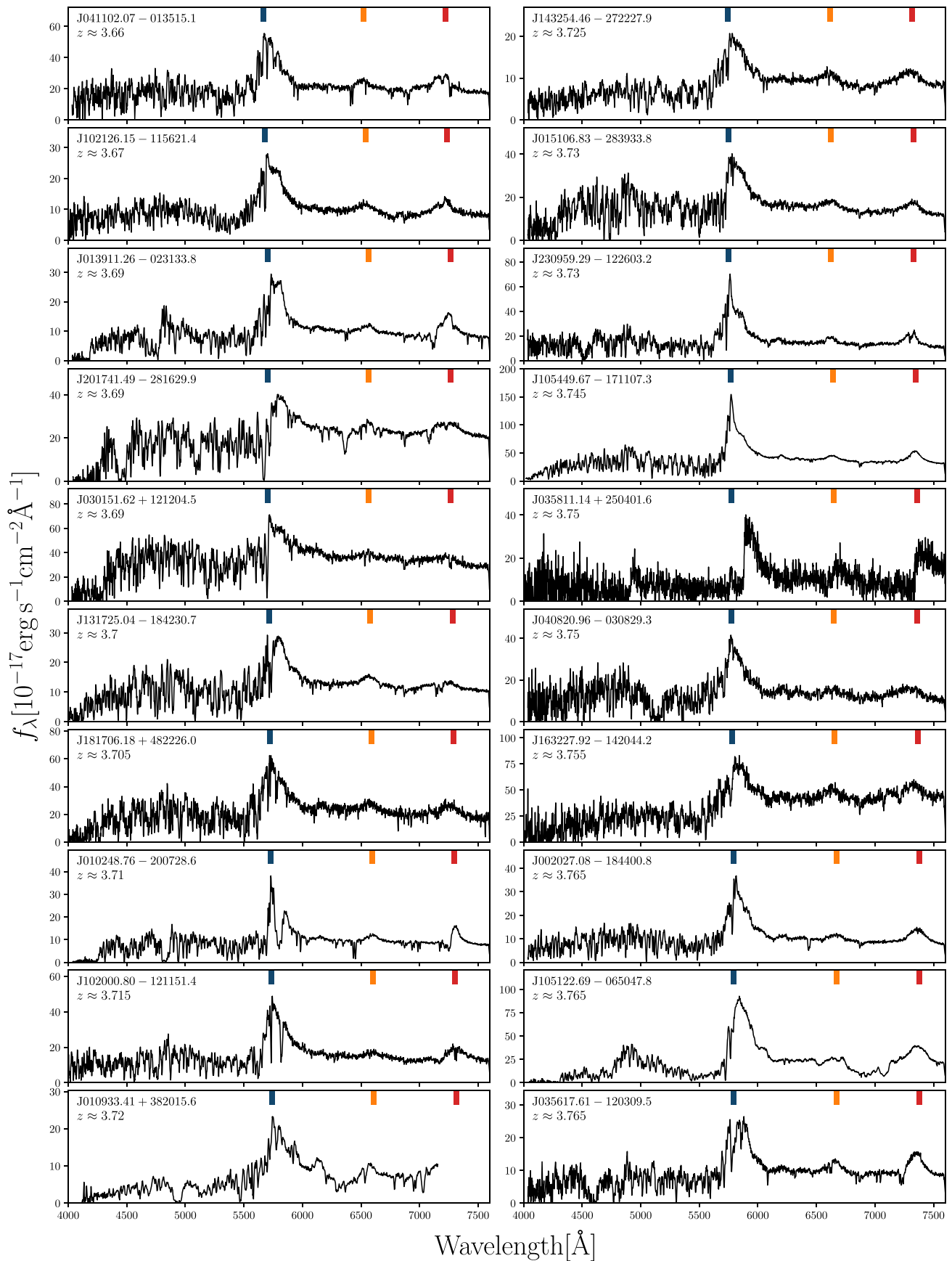


Figure 11. Discovery spectra of the newly discovered PS-ELQS quasars (continued).

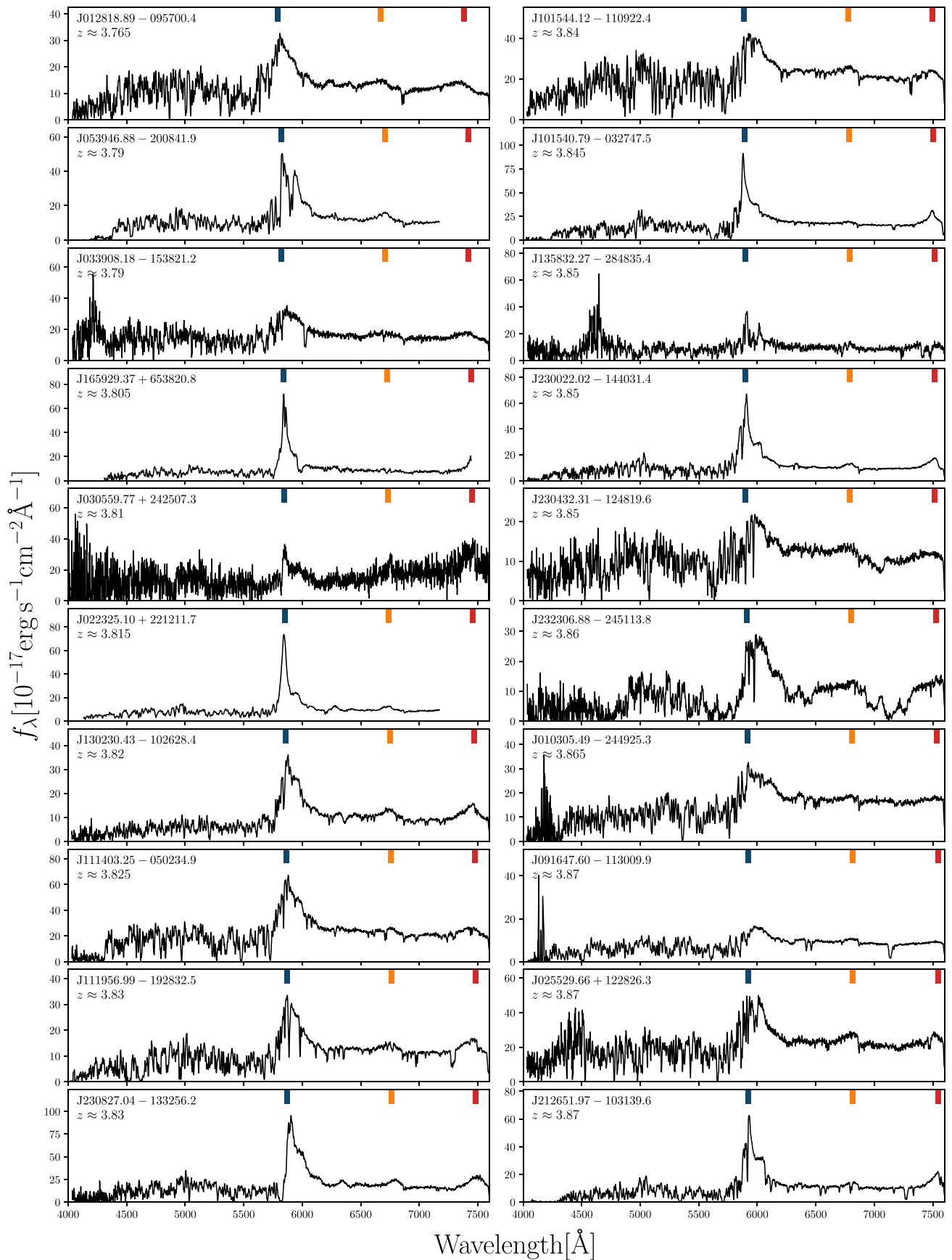


Figure 11. (Continued.)

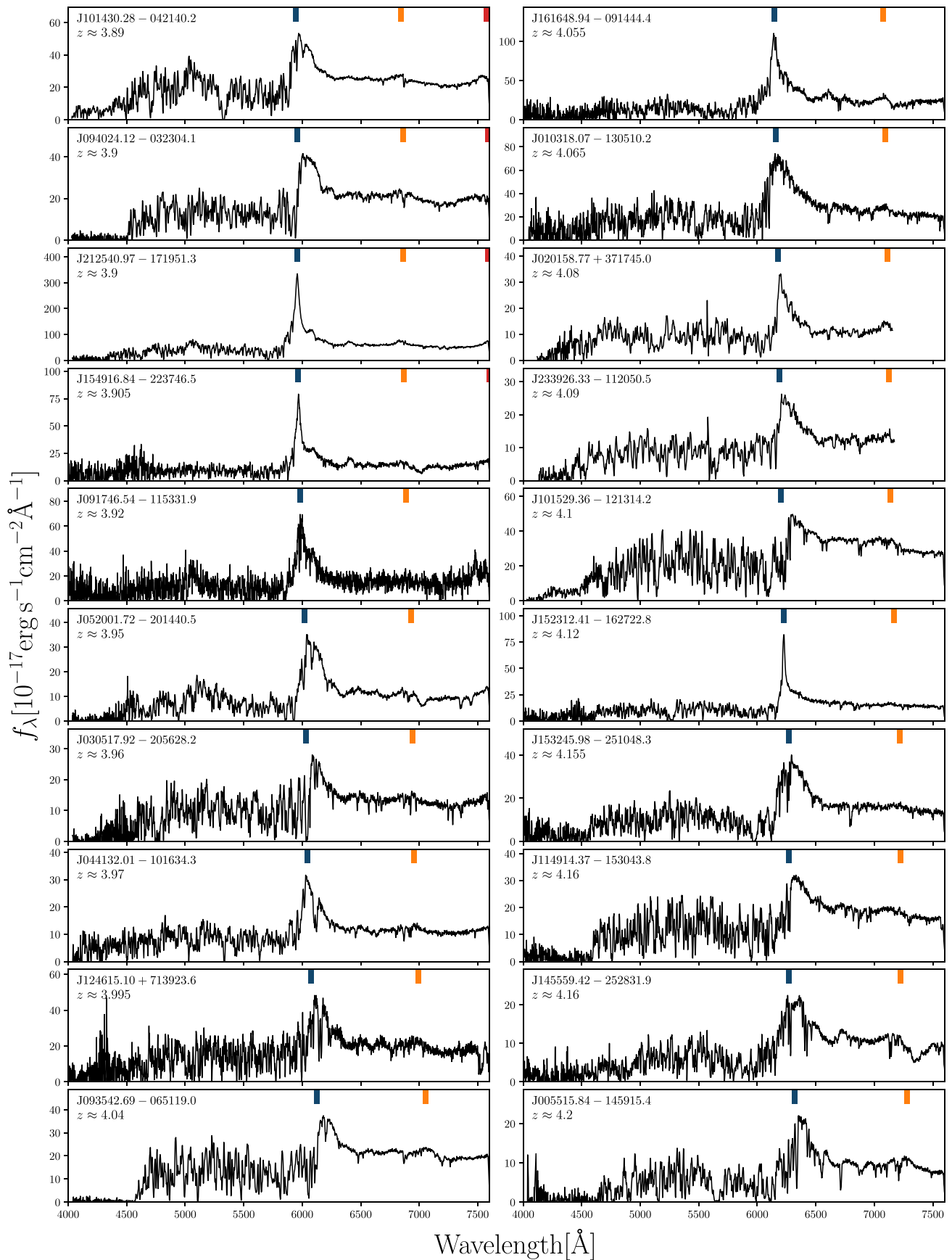


Figure 11. (Continued.)

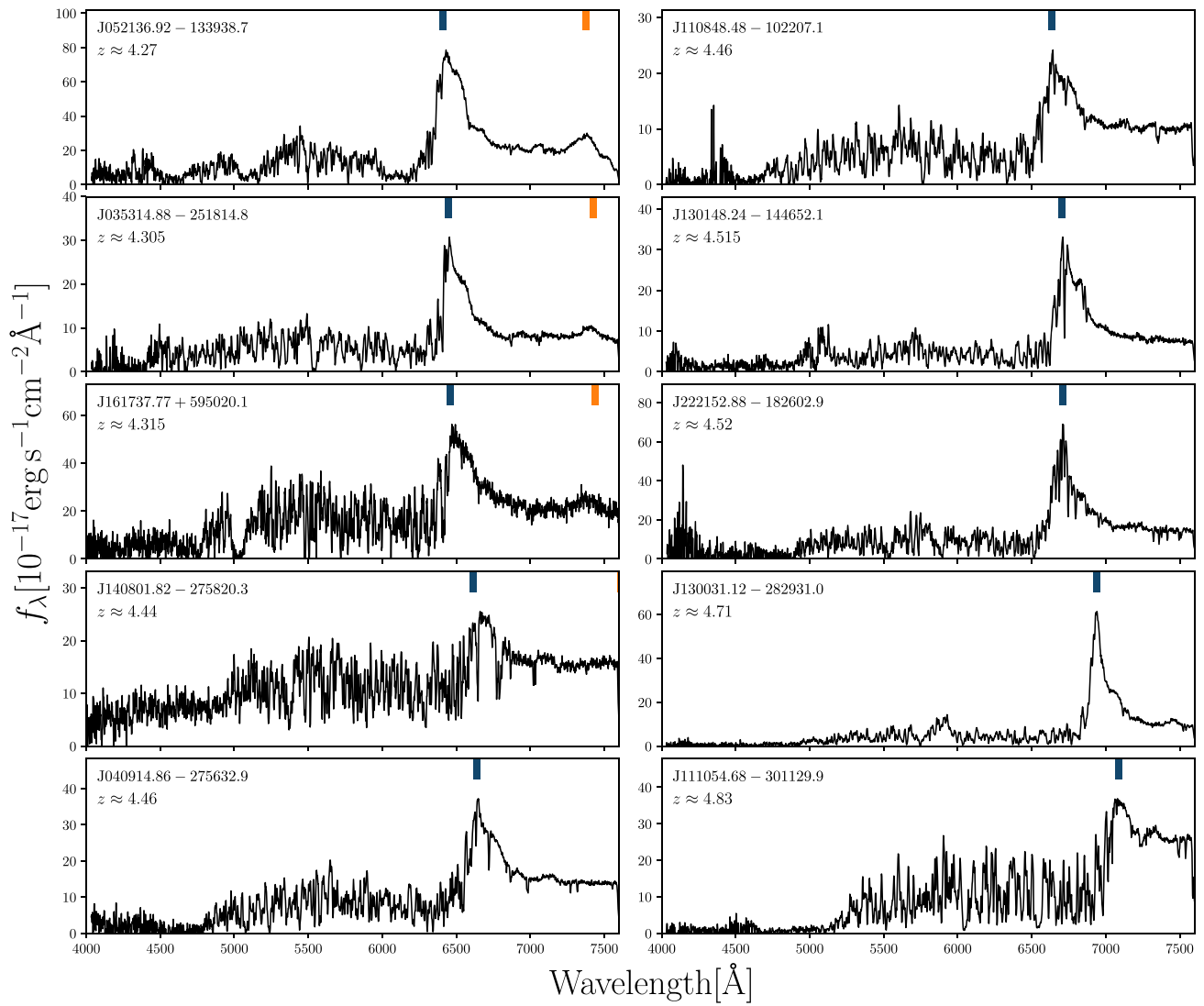


Figure 11. (Continued.)

Appendix C Newly Discovered QSOs at Lower Redshift ($z < 2.8$)

In this part of the Appendix we present newly discovered quasars targeted with PS-ELQS spectroscopically confirmed to

be at $z < 2.8$. A summary of the general properties of these objects is provided in Table 9, which is also available in machine-readable format online. The discovery spectra are shown in Figure 12.

Table 9
Newly Discovered Quasars at $z < 2.8$ in the PS-ELQS Sample

R.A. (J2000) (hh:mm:ss.sss)	Decl. (J2000) (dd:mm:ss.ss)	m_i (mag)	M_{1450} (mag)	Spectroscopic Redshift	Near-UV ^a (mag)	Far-UV ^a (mag)	Notes ^b
00:13:10.727	+29:18:47.74	17.65 ± 0.01	-27.27	2.500	171020
00:38:56.987	-29:22:24.43	17.35 ± 0.00	-27.28	2.270	180124 ^c
02:11:19.800	-19:59:43.01	17.94 ± 0.01	-26.93	2.450	171010 ^c
02:35:00.447	+02:38:29.25	18.11 ± 0.01	-23.73	0.650	180124 ^c
03:30:11.020	-12:40:08.68	17.59 ± 0.00	-26.78	2.075	171006
03:35:59.996	-13:26:02.08	17.99 ± 0.01	-26.14	1.900	171007 ^c
03:41:38.070	-11:42:59.44	17.09 ± 0.01	-27.98	2.770	171008
04:05:48.525	-24:21:15.26	17.38 ± 0.01	-27.68	2.760	171007
09:10:54.661	+46:06:51.94	18.09 ± 0.01	-26.81	2.490	180514
09:26:42.056	-17:47:21.96	18.24 ± 0.02	-22.39	0.369	20.10 ± 0.10	20.52 ± 0.17	180602
09:36:20.407	+82:51:14.07	17.54 ± 0.01	-27.50	2.715	180517
10:11:22.657	-24:33:01.43	18.12 ± 0.01	-26.92	2.720	180123
10:57:02.777	+34:22:50.37	18.08 ± 0.00	-26.63	2.320	180321
11:28:14.210	+26:56:46.36	18.18 ± 0.01	-26.32	2.170	180321
11:32:52.869	-06:32:43.31	17.68 ± 0.01	-27.15	2.410	180404 ^c
14:27:45.083	-14:51:49.32	17.79 ± 0.01	-26.96	2.350	180404
14:40:30.602	+69:42:11.58	17.99 ± 0.01	-27.04	2.690	180514
17:13:01.101	+66:58:25.90	18.29 ± 0.01	-26.67	2.550	180518
18:00:30.260	+79:34:47.07	17.93 ± 0.01	-27.12	2.755	22.06 ± 0.30	...	180518
18:03:11.956	+70:38:25.75	17.94 ± 0.01	-27.09	2.715	180518
18:07:24.633	+28:08:14.40	17.90 ± 0.00	-26.60	2.150	171020
18:20:00.261	+63:10:36.85	17.63 ± 0.00	-26.97	2.235	180518
18:29:04.759	+78:31:06.45	18.13 ± 0.01	-26.41	2.200	22.33 ± 0.35	...	180514
19:19:46.075	+74:37:47.11	17.86 ± 0.01	-25.92	1.604	180518 ^c
20:30:34.859	-25:41:57.41	18.10 ± 0.01	-26.96	2.743	180604
22:09:12.009	+06:19:20.01	17.25 ± 0.00	-26.90	1.910	171008 ^c
22:51:59.483	+17:28:44.68	17.35 ± 0.01	-27.36	2.320	180518
23:41:20.021	+31:20:25.38	18.39 ± 0.01	-26.22	2.240	171021

Notes.

^a The near and far-UV magnitudes were obtained from cross-matches within 2'' to the *GALEX* GR6/7 data release.

^b This column shows the observation date (YYMMDD) and provides further information on individual objects.

^c This object has been classified as a BAL, LoBAL, or FeLoBAL quasar. Details are discussed in Section 7.2.

(This table is available in machine-readable form.)

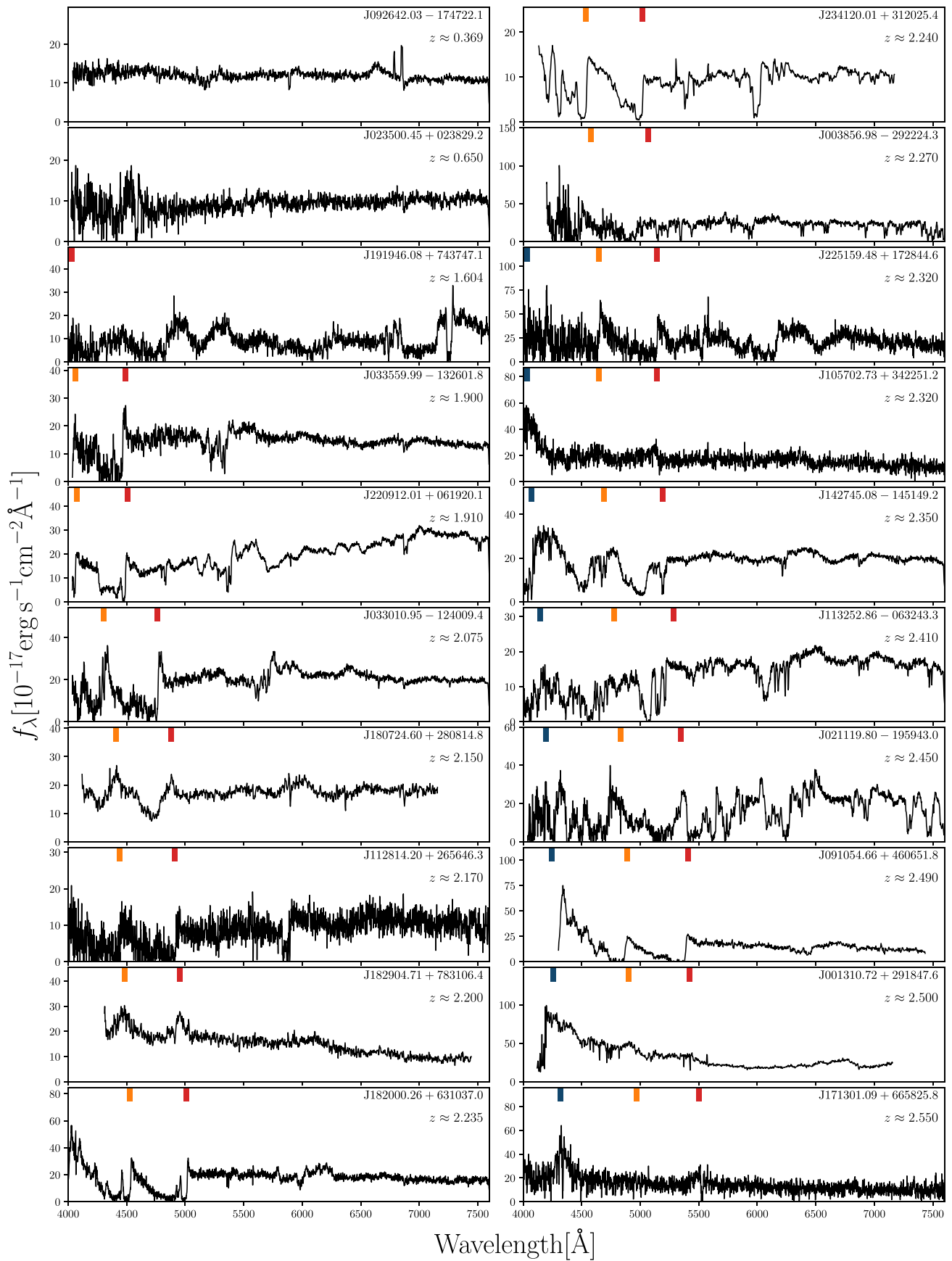


Figure 12. Discovery spectra of the newly discovered PS-ELQS quasars at $z < 2.8$. The dark blue, orange, and red bars denote the center positions of the broad Ly α , Si IV, and C IV emission lines according to the spectroscopic redshift.

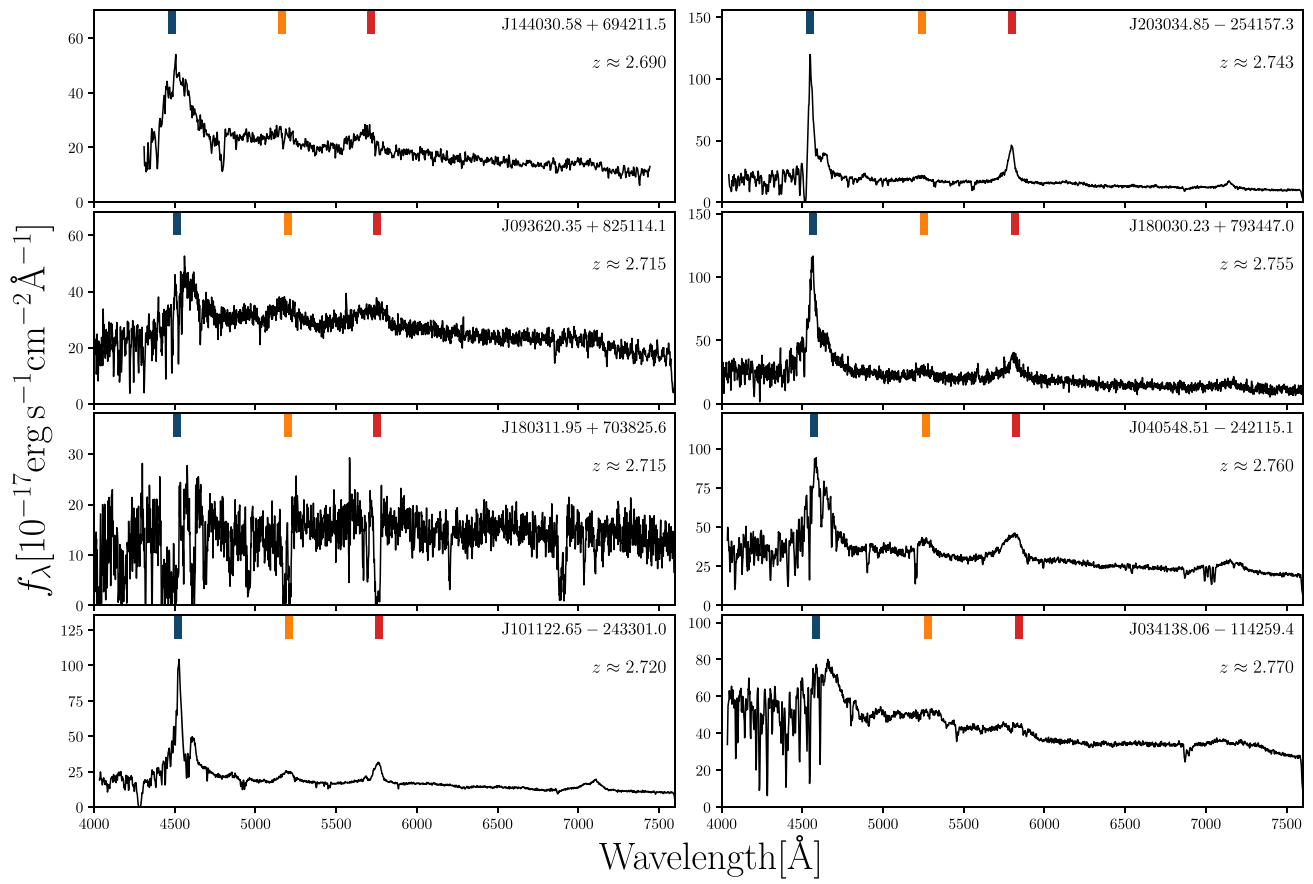


Figure 12. (Continued.)

Appendix D

Remaining Good PS-ELQS Candidates

We further present properties of the remaining good PS-ELQS candidates in Table 10. A machine-readable version of this table is provided online.

Table 10
Properties of the Remaining Good PS-ELQS Candidates

R.A. (J2000) (hh:mm:ss.sss)	Decl. (J2000) (dd:mm:ss.ss)	m_i (mag)	rf_photoz	rf_qso_prob	rf_mult_class_pred	Priority
00:08:01.926	-27:24:29.28	18.04 ± 0.01	2.83	1.00	midz	5
00:25:18.462	-15:57:50.47	18.12 ± 0.01	2.82	0.99	midz	5
00:46:12.529	+41:50:02.49	18.34 ± 0.01	3.30	0.84	highz	4
00:55:09.859	-03:49:43.89	18.32 ± 0.01	2.85	0.86	midz	5
01:54:15.903	+40:43:40.91	18.02 ± 0.01	3.59	0.86	highz	3
01:58:16.432	-01:30:38.31	18.18 ± 0.01	2.88	0.98	midz	5
02:22:07.117	-16:28:11.77	18.15 ± 0.01	2.89	0.99	midz	5
02:29:43.899	+29:33:05.50	18.34 ± 0.01	3.00	0.98	midz	5
02:39:44.591	+07:26:59.62	18.09 ± 0.00	2.92	0.73	midz	5
02:56:27.355	-18:35:49.70	18.11 ± 0.00	2.88	0.99	midz	5
03:05:33.395	+12:57:34.33	18.07 ± 0.01	2.90	0.99	midz	5
03:18:29.401	+23:34:35.21	18.32 ± 0.01	3.85	0.87	highz	3
04:14:03.285	-10:50:03.75	18.30 ± 0.01	2.83	0.98	midz	5
04:23:28.876	-27:52:23.82	18.14 ± 0.01	2.92	0.96	midz	5
04:44:07.833	+80:34:43.36	18.24 ± 0.01	3.46	0.60	highz	4
04:46:49.052	-03:54:39.44	18.48 ± 0.01	2.83	0.85	midz	5
05:05:25.937	+76:49:53.53	17.77 ± 0.01	3.58	0.94	highz	1
05:34:17.420	+75:44:13.74	17.27 ± 0.00	3.04	0.54	midz	2
05:47:06.719	+79:02:21.45	17.79 ± 0.01	3.20	0.89	midz	2
05:57:01.236	+68:30:27.86	18.14 ± 0.01	2.87	1.00	midz	5
06:12:25.946	+66:15:22.70	18.25 ± 0.01	3.15	0.90	highz	4
06:34:29.752	+56:34:42.36	18.46 ± 0.00	3.02	0.91	midz	4
06:42:53.018	+59:43:45.50	18.30 ± 0.01	3.84	0.96	highz	3
06:50:56.448	+72:53:14.65	18.04 ± 0.00	4.49	0.83	highz	3
06:52:41.984	+54:27:40.60	18.11 ± 0.02	3.65	0.99	highz	3
06:57:27.418	+57:22:11.94	17.49 ± 0.01	3.61	0.92	highz	1
07:00:32.592	+56:00:27.17	17.98 ± 0.00	3.04	0.76	highz	2
07:08:02.482	+63:15:59.67	17.20 ± 0.00	2.95	0.76	midz	3
07:14:46.848	+84:25:28.21	17.81 ± 0.01	2.93	0.64	midz	3
07:15:52.373	+42:10:06.15	17.62 ± 0.01	3.08	0.63	midz	2
07:17:03.905	+59:02:59.46	18.40 ± 0.01	3.61	0.95	highz	3
07:32:57.277	+54:52:11.55	17.80 ± 0.01	3.07	0.59	midz	2
07:37:59.176	+54:54:44.01	17.76 ± 0.00	2.88	0.96	midz	3
07:42:23.031	+68:36:31.53	18.49 ± 0.01	3.95	0.96	highz	3
07:42:58.216	+61:21:10.97	17.61 ± 0.00	3.62	0.94	highz	1
07:51:07.041	+37:11:56.34	18.19 ± 0.01	2.91	0.90	midz	5
07:51:55.122	+53:53:34.41	18.48 ± 0.00	3.50	0.92	highz	4
07:52:48.270	+70:24:33.00	18.16 ± 0.01	3.60	0.97	highz	3
07:55:50.673	+68:47:04.24	17.68 ± 0.01	2.95	0.47	midz	3
08:09:10.462	+59:01:25.22	18.23 ± 0.01	3.00	0.94	highz	5
08:23:56.195	+69:08:15.67	18.27 ± 0.00	3.21	0.95	highz	4
08:32:04.867	+57:33:15.31	18.49 ± 0.01	3.29	0.94	highz	4
13:34:19.002	+26:55:34.63	18.43 ± 0.01	3.17	0.88	highz	4
23:05:05.917	+26:47:14.04	18.27 ± 0.01	2.94	0.51	midz	5

(This table is available in machine-readable form.)

Appendix E

SQL Query to Obtain the Pan-STARRS DR1 (PS1) Photometry

We present the SQL query, which was used to obtain photometry from the Pan-STARRS DR1 catalog.

```

SELECT
m.wise_designation, m.wise_ra, m.wise_dec,
o.ObjID as PS1_ObjID, x.ra as ps_ra, x.dec as ps_dec,
o.gMeanPSFMag, o.gMeanPSFMagErr, o.gMeanKronMag, o.gMeanApMag,
o.rMeanPSFMag, o.rMeanPSFMagErr, o.rMeanKronMag, o.rMeanApMag,
o.iMeanPSFMag, o.iMeanPSFMagErr, o.iMeanKronMag, o.iMeanApMag,
o.zMeanPSFMag, o.zMeanPSFMagErr, o.zMeanKronMag, o.zMeanApMag,
o.yMeanPSFMag, o.yMeanPSFMagErr, o.yMeanKronMag, o.yMeanApMag,
o.gMeanPSFmagNpt, o.rMeanPSFmagNpt, o.iMeanPSFmagNpt, o.
zMeanPSFmagNpt, o.yMeanPSFmagNpt,
o.gFlags, o.gQfPerfect,
o.rFlags, o.rQfPerfect,
o.iFlags, o.iQfPerfect,

o.zFlags, o.zQfPerfect,
o.yFlags, o.yQfPerfect,
sp.gpetRadius, sp.rpetRadius, sp.ipetRadius, sp.zpetRadius, sp.
ypetRadius,
sot.iinfoFlag, sot.iinfoFlag2

into mydb.wise_2mass_jkw2_colorcut_matched
from mydb.wise_2mass_jkw2_colorcut AS m











CROSS APPLY (SELECT * FROM dbo.fGetNearestObjEq(m.wise_ra, m.
wise_dec, 0.066)) AS x
JOIN MeanObject o on o.ObjID = x.ObjID

LEFT JOIN StackPetrosian AS sp ON sp.objID = o.objID
LEFT JOIN StackObjectThin AS sot ON sot.objID = o.objID

WHERE (o.iMeanPSFMag > 0 AND o.iMeanPSFMag <= 19.0)
AND o.zMeanPSFMag > 0
AND o.yMeanPSFMag > 0
AND o.iQfPerfect >= 0.85 and o.zQfPerfect >= 0.85
--- rejects extended objects
AND (-0.3 <= iMeanPSFMag - iMeanApMag OR
iMeanPSFMag - iMeanApMag <= 0.3)
--- photometric quality criteria
AND (sot.iinfoFlag & 0x00000008 = 0) ---FAIL
AND (sot.iinfoFlag & 0x00000010 = 0) ---POOR/POORFIT
AND (sot.iinfoFlag & 0x00000020 = 0) ---PAIR
AND (sot.iinfoFlag & 0x00000080 = 0) ---SATSTAR
AND (sot.iinfoFlag & 0x00000100 = 0) ---BLEND
AND (sot.iinfoFlag & 0x00000400 = 0) ---BADPSF
AND (sot.iinfoFlag & 0x00000800 = 0) ---DEFECT
AND (sot.iinfoFlag & 0x00001000 = 0) ---SATURATED
AND (sot.iinfoFlag & 0x00002000 = 0) ---CR_LIMIT
AND (sot.iinfoFlag & 0x00008000 = 0) ---MOMENTS_FAILURE
AND (sot.iinfoFlag & 0x00010000 = 0) ---SKY_FAILURE
AND (sot.iinfoFlag & 0x00020000 = 0) ---SKYVAR_FAILURE
AND (sot.iinfoFlag & 0x00040000 = 0) ---MOMENTS_SN
AND (sot.iinfoFlag & 0x00400000 = 0) ---BLEND_FIT
AND (sot.iinfoFlag & 0x10000000 = 0) ---SIZE_SKIPPED
AND (sot.iinfoFlag & 0x20000000 = 0) ---ON_SPIKE
AND (sot.iinfoFlag & 0x40000000 = 0) ---ON_GHOST
AND (sot.iinfoFlag & 0x80000000 = 0) ---OFF_CHIP
AND (sot.iinfoFlag2 & 0x00000008 = 0) ---ON_SPIKE
AND (sot.iinfoFlag2 & 0x00000010 = 0) ---ON_STARCORE
AND (sot.iinfoFlag2 & 0x00000020 = 0) ---ON_BURNTOOL

```

ORCID iDs

Jan-Torge Schindler  <https://orcid.org/0000-0002-4544-8242>
Xiaohui Fan  <https://orcid.org/0000-0003-3310-0131>
Yun-Hsin Huang  <https://orcid.org/0000-0003-4955-5632>
Minghao Yue  <https://orcid.org/0000-0002-5367-8021>
Jinyi Yang  <https://orcid.org/0000-0001-5287-4242>
Patrick B. Hall  <https://orcid.org/0000-0002-1763-5825>
Lukas Wenzl  <https://orcid.org/0000-0001-5245-2058>
Allison Hughes  <https://orcid.org/0000-0002-1718-0402>
Katrina C. Litke  <https://orcid.org/0000-0002-4208-3532>
Jon M. Rees  <https://orcid.org/0000-0002-5376-3883>

References

- Abazajian, K. N., Adelman-McCarthy, J. K., Agüeros, M. A., et al. 2009, *ApJS*, 182, 543
- Aihara, H., Arimoto, N., Armstrong, R., et al. 2018, *PASJ*, 70, S4
- Akiyama, M., He, W., Ikeda, H., et al. 2018, *PASJ*, 70, S34
- Astropy Collaboration, Price-Whelan, A. M., Sipőcz, B. M., et al. 2018, *AJ*, 156, 123
- Astropy Collaboration, Robitaille, T. P., Tollerud, E. J., et al. 2013, *A&A*, 558, 33
- Bañados, E., Venemans, B. P., Decarli, R., et al. 2016, *ApJS*, 227, 11
- Bañados, E., Venemans, B. P., Mazzucchelli, C., et al. 2018, *Natur*, 553, 473
- Bañados, E., Venemans, B. P., Morganson, E., et al. 2014, *AJ*, 148, 14
- Bishop, C. M. 2006, *Pattern Recognition and Machine Learning* (Berlin: Springer)
- Boller, T., Freyberg, M. J., Trümper, J., et al. 2016, *A&A*, 588, A103
- Bovy, J., Hennawi, J. F., Hogg, D. W., et al. 2011, *ApJ*, 729, 141
- Breiman, L. 2001, *Machine Learn.*, 45, 5
- Carlíles, S., Budavári, T., Heinis, S., Priebe, C., & Szalay, A. S. 2010, *ApJ*, 712, 511
- Carnall, A. C., Shanks, T., Chehade, B., et al. 2015, *MNRAS*, 451, L16
- Carrasco, D., Barrientos, L. F., Pichara, K., et al. 2015, *A&A*, 584, A44
- Carrasco Kind, M., & Brunner, R. J. 2013, *MNRAS*, 432, 1483
- Chambers, K. C., Magnier, E. A., Metcalfe, N., et al. 2016, arXiv:1612.05560
- Chehade, B., Carnall, A. C., Shanks, T., et al. 2018, *MNRAS*, 478, 1649
- Clemens, J. C., Crain, J. A., & Anderson, R. 2004, *Proc. SPIE*, 5492, 331
- da Ángela, J., Shanks, T., Croom, S. M., et al. 2008, *MNRAS*, 383, 565
- D’Isanto, A., & Polsterer, K. L. 2018, *A&A*, 609, A111
- Dawson, K. S., Kneib, J.-P., Percival, W. J., et al. 2016, *AJ*, 151, 44
- Dawson, K. S., Schlegel, D. J., Ahn, C. P., et al. 2013, *AJ*, 145, 10
- Dubath, P., Rimoldini, L., Süveges, M., et al. 2011, *MNRAS*, 414, 2602
- Eftekhazadeh, S., Myers, A. D., White, M., et al. 2015, *MNRAS*, 453, 2779
- Eisenstein, D. J., Weinberg, D. H., Agol, E., et al. 2011, *AJ*, 142, 72
- Fan, X., Hennawi, J. F., Richards, G. T., et al. 2004, *AJ*, 128, 515
- Fan, X., Strauss, M. A., Richards, G. T., et al. 2006, *AJ*, 131, 1203
- Fan, X., Strauss, M. A., Schneider, D. P., et al. 2001, *AJ*, 121, 54
- Fan, X., Strauss, M. A., Schneider, D. P., et al. 2003, *AJ*, 125, 1649
- Fan, X., White, R. L., Davis, M., et al. 2000, *AJ*, 120, 1167
- Flesch, E. W. 2015, *PASA*, 32, e010
- Górski, K. M., Hivon, E., Banday, A. J., et al. 2005, *ApJ*, 622, 759
- Green, G. M., Schlafly, E. F., Finkbeiner, D., et al. 2018, *MNRAS*, 478, 651
- Hunter, J. D. 2007, *CSE*, 9, 90
- Jiang, L., Fan, X., Annis, J., et al. 2008, *AJ*, 135, 1057
- Jiang, L., Fan, X., Bian, F., et al. 2009, *AJ*, 138, 305
- Jiang, L., McGreer, I. D., Fan, X., et al. 2016, *ApJ*, 833, 222
- Jones, E., Oliphant, T., Peterson, P., et al. 2001, *SciPy: Open Source Scientific Tools for Python*, <https://www.scipy.org/>
- Kaiser, N., Aussel, H., Burke, B. E., et al. 2002, *Proc. SPIE*, 4836, 154
- Kaiser, N., Burgett, W., Chambers, K., et al. 2010, *Proc. SPIE*, 7733, 77330E
- Kashikawa, N., Ishizaki, Y., Willott, C. J., et al. 2015, *ApJ*, 798, 28
- Magnier, E. 2006, in *Proc. The Advanced Maui Optical and Space Surveillance Technologies Conf.*, ed. S. Ryan (Maui, HI: AMOS), E50
- Magnier, E. 2007, in *ASP Conf. Ser.* 364, *The Future of Photometric, Spectrophotometric and Polarimetric Standardization*, ed. C. Sterken (San Francisco, CA: ASP), 153
- Mainzer, A., Bauer, J., Grav, T., et al. 2011, *ApJ*, 731, 53
- Martin, D. C., Fanson, J., Schiminovich, D., et al. 2005, *ApJL*, 619, L1

- Matsuoka, Y., Iwasawa, K., Onoue, M., et al. 2018a, *ApJS*, **237**, 5
- Matsuoka, Y., Onoue, M., Kashikawa, N., et al. 2016, *ApJ*, **828**, 26
- Matsuoka, Y., Onoue, M., Kashikawa, N., et al. 2018b, *PASJ*, **70**, S35
- Matsuoka, Y., Onoue, M., Kashikawa, N., et al. 2019, *ApJL*, **872**, L2
- Mazzucchelli, C., Bañados, E., Venemans, B. P., et al. 2017, *ApJ*, **849**, 91
- McGreer, I. D., Jiang, L., Fan, X., et al. 2013, *ApJ*, **768**, 105
- McKinney, W. 2011, in Proc. 9th Python Sci. Conf., ed. S. van der Walt & J. Millman (Austin, TX: SciPy), 51
- Morganson, E., De Rosa, G., Decarli, R., et al. 2012, *AJ*, **143**, 142
- Mortlock, D. J., Warren, S. J., Venemans, B. P., et al. 2011, *Natur*, **474**, 616
- Myers, A. D., Brunner, R. J., Nichol, R. C., et al. 2007, *ApJ*, **658**, 85
- Myers, A. D., Brunner, R. J., Richards, G. T., et al. 2006, *ApJ*, **638**, 622
- Myers, A. D., Palanque-Delabrouille, N., Prakash, A., et al. 2015, *ApJS*, **221**, 27
- Oke, J. B., & Gunn, J. E. 1983, *ApJ*, **266**, 713
- Pâris, I., Petitjean, P., Aubourg, É., et al. 2012, *A&A*, **548**, A66
- Pâris, I., Petitjean, P., Aubourg, É., et al. 2018, *A&A*, **613**, A51
- Pedregosa, F., Varoquaux, G., Gramfort, A., et al. 2011, *J. Machine Learn. Res.*, **12**, 2825
- Planck Collaboration, Ade, P. A. R., Aghanim, N., et al. 2016, *A&A*, **594**, A13
- Pons, E., McMahon, R. G., Simcoe, R. A., et al. 2019, *MNRAS*, **484**, 5142
- Prochaska, J. X., Herbert-Fort, S., & Wolfe, A. M. 2005, *ApJ*, **635**, 123
- Reed, S. L., Banerji, M., Becker, G. D., et al. 2019, *MNRAS*, **487**, 1874
- Reed, S. L., McMahon, R. G., Banerji, M., et al. 2015, *MNRAS*, **454**, 3952
- Reed, S. L., McMahon, R. G., Martini, P., et al. 2017, *MNRAS*, **468**, 4702
- Richards, G. T., Fan, X., Newberg, H. J., et al. 2002, *AJ*, **123**, 2945
- Richards, G. T., Kruczek, N. E., Gallagher, S. C., et al. 2011, *AJ*, **141**, 167
- Richards, G. T., Myers, A. D., Peters, C. M., et al. 2015, *ApJS*, **219**, 39
- Rodríguez-Torres, S. A., Comparat, J., Prada, F., et al. 2017, *MNRAS*, **468**, 728
- Ross, N. P., McGreer, I. D., White, M., et al. 2013, *ApJ*, **773**, 14
- Ross, N. P., Shen, Y., Strauss, M. A., et al. 2009, *ApJ*, **697**, 1634
- Salvato, M., Buchner, J., Budavári, T., et al. 2018, *MNRAS*, **473**, 4937
- Schindler, J.-T., Fan, X., McGreer, I. D., et al. 2017, *ApJ*, **851**, 13
- Schindler, J.-T., Fan, X., McGreer, I. D., et al. 2018, *ApJ*, **863**, 144
- Schindler, J.-T., Fan, X., McGreer, I. D., et al. 2019, *ApJ*, **871**, 258
- Schlegel, D. J., Finkbeiner, D. P., & Davis, M. 1998, *ApJ*, **500**, 525
- Schmidt, T. M., Hennawi, J. F., Lee, K.-G., et al. 2018, arXiv:1810.05156
- Schneider, D. P., Richards, G. T., Hall, P. B., et al. 2010, *AJ*, **139**, 2360
- Shen, Y., Strauss, M. A., Oguri, M., et al. 2007, *AJ*, **133**, 2222
- Simcoe, R. A., Sargent, W. L. W., & Rauch, M. 2004, *ApJ*, **606**, 92
- Timlin, J. D., Ross, N. P., Richards, G. T., et al. 2018, *ApJ*, **859**, 20
- Tody, D. 1986, *Proc. SPIE*, **627**, 733
- Tody, D. 1993, in ASP Conf. Ser. 52, *Astronomical Data Analysis Software and Systems II*, ed. R. J. Hanisch, R. J. V. Brissenden, & J. Barnes (San Francisco, CA: ASP), 173
- Truemper, J. 1982, *AdSpR*, **2**, 241
- Vanden Berk, D. E., Richards, G. T., Bauer, A., et al. 2001, *AJ*, **122**, 549
- Venemans, B. P., Findlay, J. R., Sutherland, W. J., et al. 2013, *ApJ*, **779**, 24
- Venemans, B. P., McMahon, R. G., Warren, S. J., et al. 2007, *MNRAS*, **376**, L76
- Volonteri, M. 2012, *Sci*, **337**, 544
- Wang, F., Yang, J., Fan, X., et al. 2018a, arXiv:1810.11926
- Wang, F., Yang, J., Fan, X., et al. 2018b, *ApJL*, **869**, L9
- White, M., Myers, A. D., Ross, N. P., et al. 2012, *MNRAS*, **424**, 933
- Willott, C. J., Delorme, P., Omont, A., et al. 2007, *AJ*, **134**, 2435
- Willott, C. J., Delorme, P., Reylé, C., et al. 2010, *AJ*, **139**, 906
- Worseck, G., & Prochaska, J. X. 2011, *ApJ*, **728**, 23
- Worseck, G., Prochaska, J. X., Hennawi, J. F., & McQuinn, M. 2016, *ApJ*, **825**, 144
- Wu, X.-B., Hao, G., Jia, Z., Zhang, Y., & Peng, N. 2012, *AJ*, **144**, 49
- Wu, X.-B., & Jia, Z. 2010, *MNRAS*, **406**, 1583
- Yang, J., Wang, F., Fan, X., et al. 2019a, *AJ*, **157**, 236
- Yang, J., Wang, F., Fan, X., et al. 2019b, *ApJ*, **871**, 199
- York, D. G., Adelman, J., Anderson, J. E., Jr., et al. 2000, *AJ*, **120**, 1579